



Erasmus+



Erasmus Mundus Joint Master degree
Photonics for Security Reliability and Safety



Master Photonics *for Security Reliability and Safety* (PSRS)



POLITECNICO
DI TORINO

RESISTIVE SWITCHING IN MOTT MATERIALS Master Thesis Report

Presented by
Tushar Chakrabarty

and defended at the
University Jean Monnet

30th August, 2023

Academic Supervisor: Dr. Carlo Ricciardi

Host Supervisor: Dr. Pascale Diener

Jury Committee:

Giraud Pascal

Dr. Carlo Ricciardi

RESISTIVE SWITCHING IN MOTT MATERIALS

Master Thesis Report

Tushar Chakrabarty

August, 2023

Master Photonics for Security Reliability and Safety (PSRS)

Abstract

Mott materials are a class of correlated materials which undergo resistive switching by creating a metallic filament between electrodes under the presence of an electric field. Such resistive switching has potential application in resistive random access memories and artificial neuron. For its use in electronic devices, it is necessary to characterize the switching time and energy necessary for the transition which have not been almost studied yet. Additionally, it is also crucial to understand about the geometry, conductivity, chemical composition of filaments on a nanoscale. So in the first part of the work, we experimentally determined the switching energy for the resistive switching in GaMo_4S_8 narrow gap Mott materials at 250 K, which fluctuates depending on the electric field between 313 μJ and 112 μJ . Furthermore, a simple model is put out to estimate the characteristic transition energy per volume, which is 25 $\text{pJ}/\mu\text{m}^3$. The final part of the work is dedicated to the characterization and understanding of a permanent filament created by a small electric field pulse for small, micrometric interelectrode distances. The filament was found to be conductive and trench shaped by the C-AFM characterization. Further examination using EDX and Raman characterization revealed that the filament has gone through a chemical change thus corresponding to a specific irreversible resistive transition rather than a non-volatile Mott transition.

Acknowledgement

I want to express my gratitude to **Dr. Pascale Diener** for allowing me to conduct research on this subject under her guidance. Working on this fascinating experimental project has been a very interesting journey from the start to the present. I would like to thank **Dr. Yevheniia Chernukha** for her technical assistance and supervision with the electrical characterization in cryostat and nanoprobe during this internship.

I also appreciated **David Troadec** for the EDX measurement and **Dr. Louis Thomas** for instructing me on the AFM platform. Moreover, I want to thank **Houda Koussir, Huu Thoai Ngo** and the whole Physics group at IEMN for their support and encouragement throughout the entire time.

Finally, and most importantly, I would like to express my gratitude to the entire **PSRS team**. It's been a great two years. Thank you all.

August, 2023, Lille, France.

Tushar Chakrabarty

Table of Contents

Abstract	i
Acknowledgement	ii
Chapter 1 Introduction	1
1.1 Mott Materials	1
1.2 Crystal Structure	4
1.3 IMT transition in AM_4Q_8 compounds	5
1.4 Research gap and contribution of this thesis	10
Chapter 2 Experimental Techniques	11
2.1 Cryogenic Electrical Setup	11
2.1.1 Setup for Transport Measurements	14
2.1.2 Setup for Resistive Switching Measurements	15
2.2 Nanoprobe	16
2.3 Characterization technique	17
2.3.1 Conductive atomic force microscopy (C-AFM)	17
2.3.2 Energy-dispersive X-ray spectroscopy (EDX)	19
2.3.3 Raman Spectroscopy	20
Chapter 3 Volatile Transition	23
3.1 Studied Samples	23
3.2 Transport Measurement at low electric field	24
3.3 Non-linear transport and electrical threshold	25
3.4 Switching & Delay Time	26
3.5 Switching Power and Energy	28
3.6 Modelling of Switching Phenomenon	30
3.7 Artificial Neuron	32
Chapter 4 Filament Characterization	35
4.1 Filament Creation	35
4.2 C-AFM characterization	37
4.3 EDX characterization	40
4.3 Raman characterization	42
Conclusions & Future Work	45
References	46
Statement of non-plagiarism	50

Supervisor approval	51
Copyright of Figures.....	52

Chapter 1 Introduction

The world is entering the era of machine learning and internet of things which is growing the demand of high computing power. But currently all the computers are based on von Neumann architecture where the memory and computing unit are separated which limits the computing ability. To cope with this problem, a lot of research have been done on biological neuron inspired neuromorphic computing to implement an in memory computing architecture.

Recently, Mott materials have been a topic of great interest among the researchers because of its potential to replicate a biological neuron type behaviour [1]–[3]. This type of materials changes phases from an insulator to a metal depending on various stimuli such as temperature, pressure or voltage [4]. Moreover, this transition can be controlled efficiently by controlling the applied voltages which make it a potential candidate to be used both as a memory [5] and an artificial neuron [6]. This kind of transitions can be temporary or permanent depending on the applied electric field and thus it is interesting to observe the temporary (volatile) and permanent (non-volatile) switching. When a pulse exceed the threshold electric field, this switching does not happen instantaneously. Instead, it happens sometime after the beginning of the pulse. This duration of time is called delay time. Already a lot of researches have been done on different Mott materials but we will focus our master thesis on GaTa_4Se_8 and GaMo_4Se_8 narrow gap Mott materials to observe this switching phenomenon.

From the next section we will simultaneously explain few background and discuss the corresponding state of the art of research that have been done so far. Then we will focus on some research gap and discuss on those open questions throughout this report.

1.1 Mott Materials

Electrical conductivity is one of the fundamental properties of a material. Depending on this property, a material can be defined as insulator, semiconductor or conductor. Experimentally, this property can be easily measured and generally band theory is used to theoretically explain this property. According to band theory, if the valence and conduction bands overlap then the material is expected to be conductor. On the other hand, if the energy gap between this two bands is greater than 3 eV, then an insulating behaviour is expected. For a semiconductor, this energy gap is below few eV, typically 3 eV. A typical example of semiconductor is Si which shows an energy gap of 0.7 eV. The schematic presentation of band structure for insulator, semiconductor and conductor is shown in Fig. 1.1.

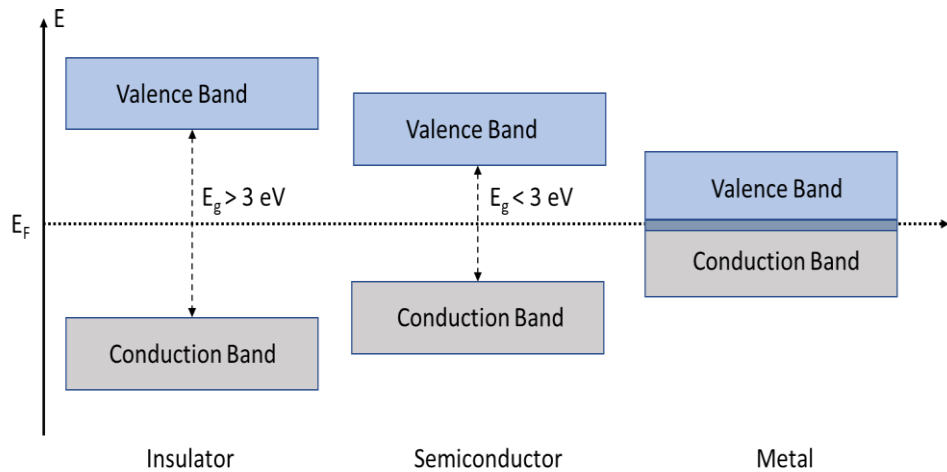


Figure 1.1 Energy band of insulator, semiconductor and metal

In conventional band theories, interactions between electrons are neglected. Thus, according to this theory, a half filled band is considered as conductor whether a full filled band is predicted to be an insulator. But in reality, there exists some material which shows insulating behaviour having a half filled band due to the strong electron correlation. These materials are called Mott insulators. The Mott insulating behaviour and some insulator to metal transitions (IMT) observed in these materials can be explained by the Hubbard model [7].

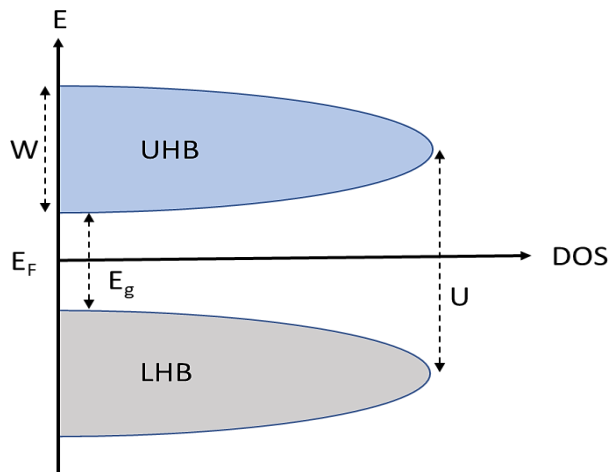


Figure 1.2 Split energy band of Mott material

According to this model, the half-filled band (one electron per site) splits into two sub-bands having bandwidth W due to the presence of a strong electron repulsion energy U as shown in Fig. 1.2. Depending on the influence of W and U , the Mott material can show insulating and metallic characteristics.

Several types of IMT are observed in these materials. In bandwidth controlled or pressure induced IMT, the external pressure increases the value of the bandwidth, W which modifies the correlation strength U/W and the orbital overlaps as shown in Fig 1.3. This causes the transition of Mott materials from an insulating to a metal phase.

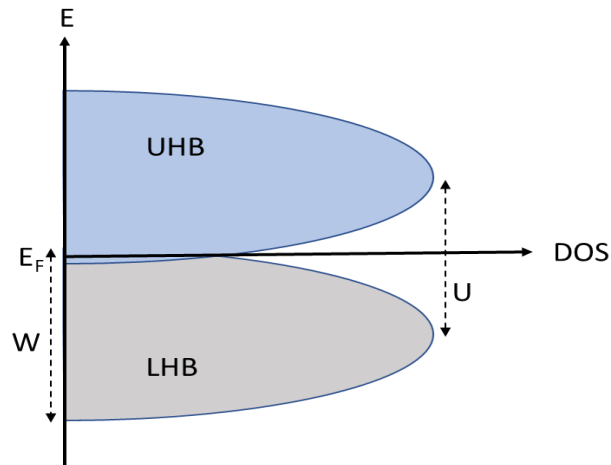


Figure 1.3 Energy band diagram for pressure induced (bandwidth controlled) Mott IMT

On the other hand, in filling controlled IMT the transition to the metal phase can be obtained by deviating from the half-filled band. This can be achieved by hole or electron doping to change the number of occupied sites which in turns alter the Coulomb repulsion. The corresponding energy band diagram for filling controlled IMT are shown in Fig. 1.4 for both electron and hole doped case.

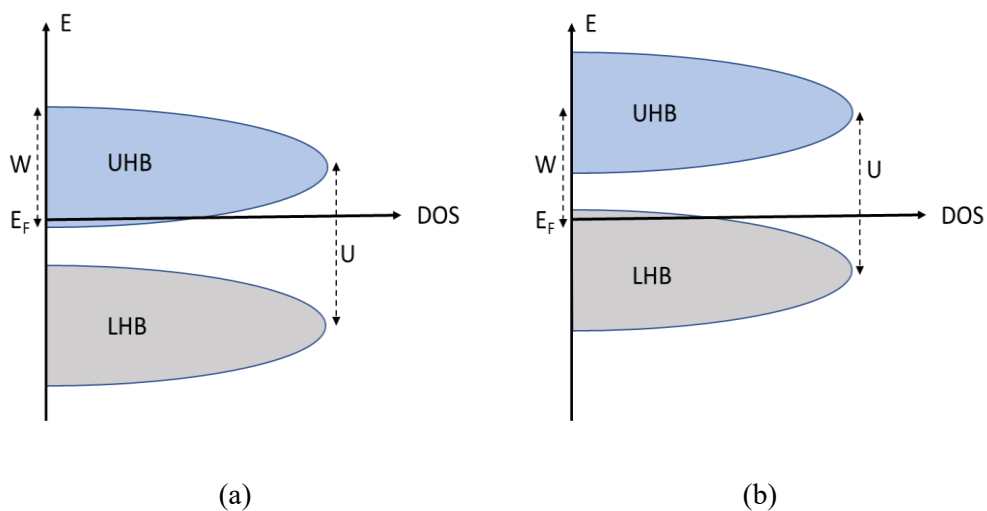


Figure 1.4 Energy band diagram for filling controlled IMT (a) electron doped; (b) hole doped

1.2 Crystal Structure

Several material such as VO_2 , NbO_2 , MnO show Mott transitions. In this master thesis, we focus on the narrow gap Mott insulators AM_4Q_8 ($A = \text{Ga, Ge}$; $M = \text{V, Mo, Ta}$; $Q = \text{S, Se}$) family and specially on GaMo_4S_8 and GaTa_4Se_8 single crystals.

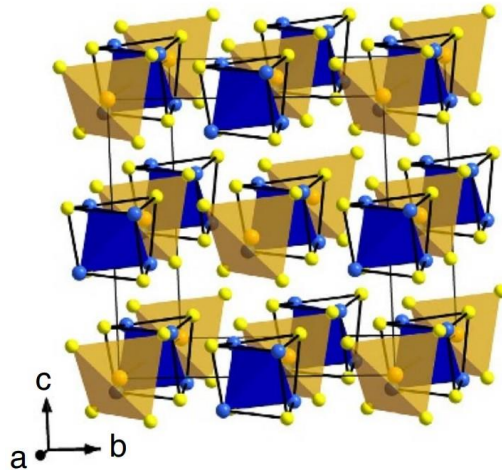


Figure 1.5 Crystal structure of AM_4Q_8 family (Orange : A, Blue : M, Yellow : Q) [8]

The AM_4Q_8 family exhibits a lacunar spinel structure with tetrahedral metal clusters M_4 (marked as blue area) [8] as shown in Fig. 1.5. Each cluster contains one unpaired electron and thus it is predicted to be metallic in nature. But these clusters are also responsible for the correlation phenomenon and the correlation takes place between each cluster. A schematic of this is provided in Fig. 1.6 where the Coulomb interaction is shown between the unpaired electron of distinct clusters. As the interaction is on the cluster level, this reduces the Coulomb interaction compared to other Mott insulators where the interaction is on the atomic scale [9]. This in returns make this type of Mott insulators to tune easily through the IMT.

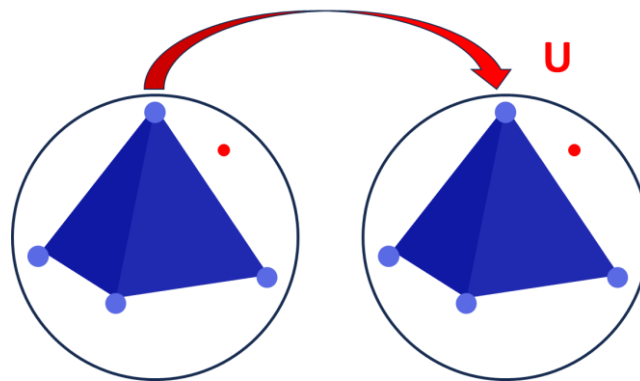


Figure 1.6 Coulomb interaction between M_4 clusters (The unpaired electrons are shown in red)

1.3 IMT transition in AM_4Q_8 compounds

The IMT transition in AM_4Q_8 family can be done by temperature, pressure and doping, but also by applying an electric field. This section summarizes what have been already reported in the literature about these IMT transitions.

The AM_4Q_8 compounds show some interesting nature as they are paramagnetic above 55 K [10] and do not go through temperature controlled IMT below 800 K at normal pressure [4]. But by increasing the pressure, this compound can go through bandwidth controlled IMT. Phuoc et al. have observed this type of insulator to metal transition at 6 GPa in $GaTa_4Se_8$ crystals by optical conductivity measurement [11] and Camjayi et al. found the transition at 5 GPa by resistivity (transport) measurement [12]. Another interesting characteristics of $GaTa_4Se_8$ crystal has also been observed by Park et al. that this compound can also show a superconductivity nature at high pressure if the temperature is cooled below 5.8 K [13].

Though this kind of transitions are possible but it is not so feasible to realize an electronic device using filling or bandwidth controlled IMT. Because of this, an electric field controlled IMT is more suitable and interesting in terms of practical implementation. Hence, throughout this report we will focus on this type of transitions. Generally, when an electric field is higher than a threshold value, AM_4Q_8 compounds go through a dielectric breakdown and the resistance drops. This means that the material goes through a resistive switching. If the applied electric field is not very high compared to the threshold, the material goes back to initial resistance state when the electric field is removed. This is known as volatile switching. On the other hand, if the applied electric field is very high (around 5 times of threshold), this transition can be permanent and the resistance remains low even if the field is removed. This type of permanent transition is called non-volatile switching. This dielectric breakdown scenario in Mott insulators can be explained by a model adapted from a theory proposed by Fröhlich for conventional semiconductors. In this theory, two regimes of dielectric breakdown are distinguished, the clean and the dirty limits. In the clean regime, the electrons in the conduction band are accelerated by the electric field and due to impact ionization it leads to a lot of free carriers and this gain is limited only by the electron phonon scattering. But in the dirty limit, we have to consider the electron-electron scattering also. This situation actually arises in the case of Mott insulators.

According to this model, the trapped electron has a ground value ϵ_0 , several electrons N_i (marked blue) are distributed in a range $\Delta\epsilon$ near below the conduction band and some electron N_c occupy conduction band as shown in Fig. 1.7 (a). These trapped electrons N_i cannot be accelerated by electric field but they are responsible for the electron-electron scattering in the dirty limit. Fig. 1.7 (b) shows the simulated density of state (DOS) of a doped $GaTa_4Se_8$ compound which show similar peak just below the conduction band. This means that it has some trapped electrons which are same as Fig. 1.7 (a) and thus the dirty limit breakdown explanation can be used for this type of Mott materials.

The breakdown mechanism is based on the thermal balance of the electronic system. As shown in Fig. 1.7 (c), the electrons in the conduction band gain energy (P_A) and they are scattered with the trap electrons. This increases the electronic temperature T_e from lattice temperature T_0 . Simultaneously, these trap electrons also interact with the phonon and this loss term reduces the electronic temperature. Thus, when both the gain and loss are in equilibrium, the electronic temperature becomes constant as shown in Fig. 1.7 (d). But if the electric field, E is higher than the threshold value, E_{th} then the gain term overshoots the loss term and they do not reach equilibrium. Rather, the temperature increases rapidly and causes the breakdown as indicated in Fig. 1.7 (d).

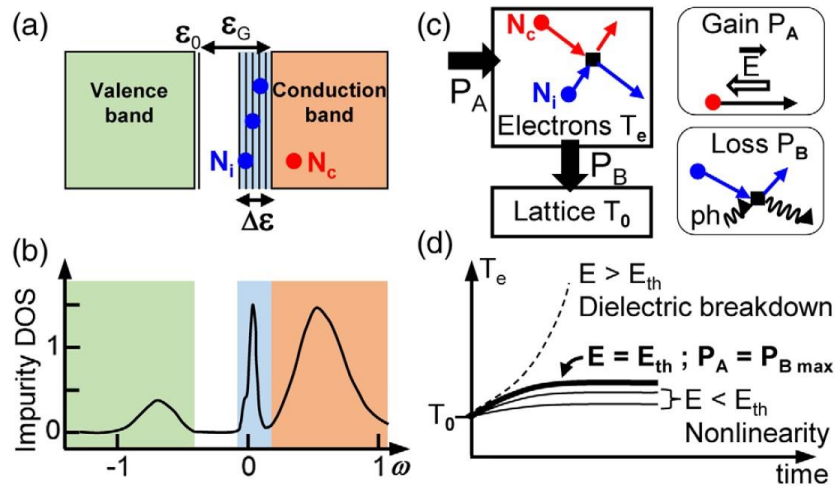


Figure 1.7 Schematic of dielectric breakdown (a) DOS according to Frohlich model; (b) Simulated DOS of Mott insulator GaTa4Se8; (c) Thermal balance of the electronic system; (d) Electronic temperature evolution for different electric field [14]

Generally, this threshold electric field, E_{th} depends on temperature, T of the material and the relation is given by [14]

$$E_{th} \propto \exp\left(\frac{\Delta\epsilon}{4KT}\right) \quad (1.1)$$

Where $\Delta\epsilon$ is the width of the impurities energy levels and K is the Boltzmann constant.

When this dielectric breakdown occurs in GaTa₄Se₈ and GaMo₄Se₈ compounds, a conductive metallic filament is created between the electrodes. Janod et al. modelled this phenomenon by a series of resistive network [15]. According to this model, the Mott insulator can be represented by a set of block of resistors (cells) shown in Fig. 1.8 and each of this cell can be in a Mott insulating (MI) or a correlated metallic (CM) state. The MI state represents the higher resistance R_{MI} and the CM state represents the lower resistance R_{CM} . Besides, the CM state has a higher energy than the MI state

($E_{CM} > E_{MI}$) and the difference between these two energy is E_D ($E_D = E_{CM} - E_{MI}$). The transition of one cell from the MI state to the CM is state is possible by an application of an electric field which provides the sufficient energy for this transition. On the other hand, the cell can also return to its MI state by relaxation.

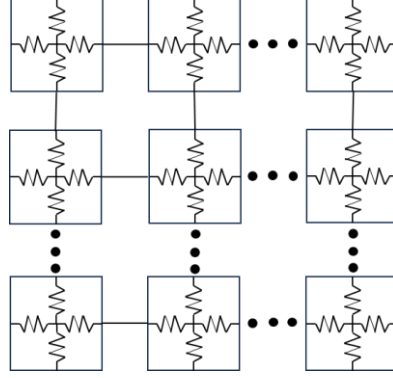


Figure 1.8 2D resistive network representation of Mott insulator

The transition probability, $P_{MI \rightarrow CM}$ (MI state to the CM state) and relaxation probability, $P_{CM \rightarrow MI}$ (CM state to the MI state) given by the following equations [4]:

$$P_{MI \rightarrow CM} = A \exp\left(\frac{-E_D + q|\Delta V|}{KT}\right) \quad (1.2)$$

$$P_{CM \rightarrow MI} = A \exp\left(\frac{-E_D + E_M}{KT}\right) \quad (1.3)$$

Here, A is attempt rate, K is Boltzmann constant, T is temperature, q is the charge of electron and ΔV represents the voltage drop in one cell. If the transition probability overcomes the relaxation probability, then metallic cells are accumulated and a conductive filament is created. In such a way, the resistive switching happens and this filament can be permanent if the applied electric field is comparatively higher than the threshold. This model explains that increasing electric field accelerates the formation of the filament and thus reduces the delay time of the switching. But in this model, the relaxation term is fixed and the voltage drop at metallic cells are negligible compared to the drop at insulating cells.

So, Tesler et al. extended this model by adding an elastic energy term E_{EL} with E_D which changes the previous transition probability as follows: [16]

$$P_{MI \rightarrow CM} = A \exp\left(\frac{-E_D - E_{L(MI)} + q|\Delta V|}{KT}\right) \quad (1.4)$$

$$P_{CM \rightarrow MI} = A \exp\left(\frac{-E_D - E_{L(CM)} + E_M}{KT}\right) \quad (1.5)$$

This elastic energy term $E_{L(CM)}$ and $E_{L(MI)}$ comes from the structural strain generated at the boundary between metallic and insulating cells. According to this model, this elastic energy term is zero if the surrounding cells are in different states compared to the initial state of the corresponding cell. But the elastic energy terms becomes $2kQ$, where k is elastic constant and Q represents the number of cells those are in similar state of the corresponding cell.

As an example, let's consider that initially the corresponding cell (red boundary) is in MI state and surrounding or nearest neighbour cells are in a CM state as shown in Fig. 1.9 (a). Here, the white cell and blue cell represent the MI state and CM state respectively. So, after the transition the corresponding cell will be in CM state and hence there will be no elastic energy from the boundary of these cells. Thus, in this condition the elastic energy, $E_{EL} = 0$. On the other hand, if 2 nearest neighbour cells of the corresponding cells are in the same state of the corresponding cell, then the elastic energy, $E_{EL} = 4k$. The corresponding figure is shown in Fig. 1.9 (b).

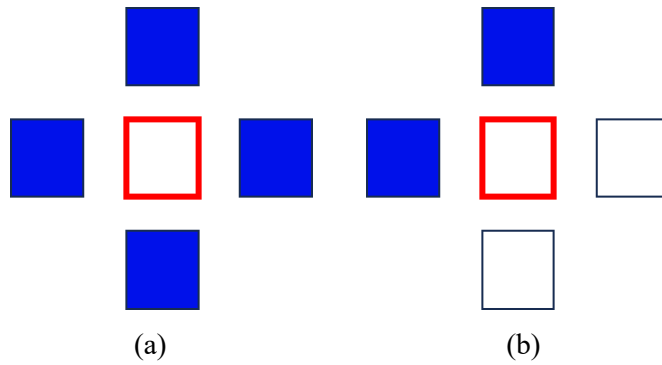


Figure 1.9 Explanation of elastic energy (a) all neighbours are in different state; (b) 2 neighbours are in same state (red boundary represents the corresponding cell)

The important feature of this model is that it can explain the filament formation and successive thickening of the initially created filament if more electric pulse is applied. Using the elastic energy term, we can explain this phenomenon. We know that if the adjacent or neighbouring cells are in different state with respect to the corresponding cell, then the elastic energy term is zero. So according to this mode, if the adjacent cells are in CM state, then less energy is required to turn the corresponding MI state cell to transform into the CM state. Thus, it explains that if we continue to apply an electric field after the first filament formation, the filament will continue to be thicker which was experimentally observed by Janod et. al. [4]. Besides, the growth of the filament follows a dynamics which depends on the evolution of the number of CM state cells with time and it is expressed as the sum of two terms [16]. In this following expression, the first term on the right hand side represents a gain term and the second one corresponds to a loss term.

$$\frac{dn_{CM}}{dt} = [n_{MI}P_{MI \rightarrow CM}] - [n_{CM}P_{CM \rightarrow MI}] \quad (1.6)$$

Here, n_{CM} and n_{MI} represents the number of CM and MI states cell respectively. At a particular value of applied voltage these two terms cancel each other and the system enters into an equilibrium condition. This particular value of applied voltage is known as the threshold voltage, V_{th} and as we increase more than this voltage the gain term overshoots the loss term and the number of MI cells increase rapidly to form a filament. With increasing applied voltage, the gain term overcomes the loss term quickly that causes faster formation of filaments and thus reducing the delay term.

But if the electrical pulse or applied voltage is removed, the filament goes under relaxation and the rupture of the filament is observed. The CM state cells relaxes and goes back to its initial MI state but here the elastic energy also have an influence on the relaxation time. If the corresponding CM state cell, which goes under relaxation is on the border i.e. surrounded more by the MI state cells have a higher probability of relaxing back to the MI state as it will face less elastic energy on this transition. As shown in Fig. 1.10, we can see the filament in blue colour whereas the outside cells are insulating (MI state). Hence, the cell marked in the border of the filament (yellow marked) has more probability to return back to MI state compared to the cell that is in the middle of the filament (red marked).

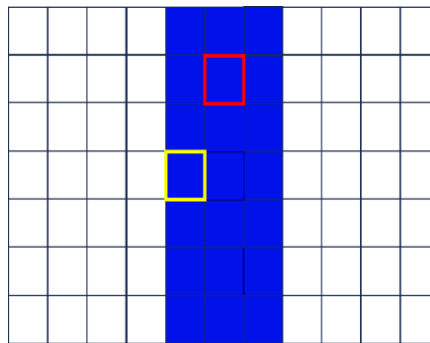


Figure 1.10 Cell relaxation illustration of a filament.

The electrically induced resistive switching i.e. creation of metallic filaments in Mott materials under electric pulses make it a possible candidate for several applications. One of its prominent applications can be on the resistive random access memory (ReRAM) as the Mott material shows non-volatile switching. This has already been demonstrated at room temperature using GaV_4S_8 thin films and two distinct resistance state could be obtained using ± 2.5 V amplitude and $10 \mu s$ pulse [17]. Another type of application can be on neuromorphic computing to implement an artificial neuron that can mimic the leaky integrate and fire behaviour. This has also been reported by several studies in AM_4Q_8 materials [1]- [3]. Because of this application in microelectronics, it is important to know about the resistive switching with a more depth analysis and in the next section we will introduce the open question that is need to be investigated.

1.4 Research gap and contribution of this thesis

So far we have discussed about how a IMT transition can happen in a Mott material, several findings and modelling that have been done so far to explain this phenomenon. The resistive switching with electric field in AM_4Q_8 Mott materials has been reported experimentally by electric field through experiment [18]–[20] and have been partially explained with resistive network models [4],[9],[16]. It is well established that the delay time for the resistive switching is decreasing with the amplitude of the pulse. However, the definition of this delay time is varying from one study to another and a clear methodology to determine this characteristic time is lacking. Moreover, the energy required for the switching has not been investigated. But this is an important feature to be analysed when we are thinking about the potential application of this material in the neuromorphic and microelectronics industry .

Besides, very few studies have been reported on the observation of this switching at the nanoscale. Dubost et al. observed the change of morphology on $GaTe_4Se_8$ crystal using the scanning tunnel microscopy (STM) tips and found some local conductive, insulating and super insulating zones [21]. Motivating from this, we want to go further by creating a permanent conductive filament on the top surface of the $GaMo_4S_8$ crystal using electrode and analyse the morphology and conductance of this filament by a conductive atomic force microscopy (C-AFM).

So, the following questions are to be answered in this thesis by experimental approach:

- 1) How is the delay time associated with the input electric pulse and how much energy is required to achieve the volatile switching?
- 2) What is the morphology and conductance of the metallic filament created on the top surface of the $GaMo_4S_8$ crystal by the non-volatile switching?

To do so, the next chapter will be devoted to explain about the instrument and experimental details. Then the results from the volatile resistive switching experiments and filament characterization will be provided in 3rd and 4th chapter respectively to find out the answer of aforementioned questions. Finally, the report will be concluded by summarizing the result and future work.

Chapter 2 Experimental Techniques

This chapter will address the experimental methodologies used in this thesis. First, we will discuss about the cryogenic electrical transport setup and how it was adapted for the characterization of single crystals. Then, we will discuss about the preparation of crystal sample (Mott materials) and the nanoprobe setup. Finally, we will discuss about the characterization technique such as atomic force microscope (AFM), Energy-dispersive X-ray spectroscopy (EDX) and Raman spectroscopy which will be done on the studied sample to characterize the resistive switching at nanoscale.

2.1 Cryogenic Electrical Setup

The cryogenic setup is made of a liquid nitrogen reservoir (cryostat) in thermal contact with the sample. Measurements can be done down to 78 K and up to 500 K thanks to a resistive heater and precise control of the temperature is performed with the help of Lake Shore Model 336 temperature controller.

A picture of this cryostat is shown in Fig. 2.1 where vacuum is created inside the chamber by pumping out the air through the vacuum port. Later the vacuum inside the first stage is ensured by closing the vacuum valve. To cool down the cryostat, liquid nitrogen is provided on the second stage through the nitrogen entry tube and a lowest 78 K can be obtained in the cryostat. There are also 4 electrical ports which are connected to the inner 4 electrodes.

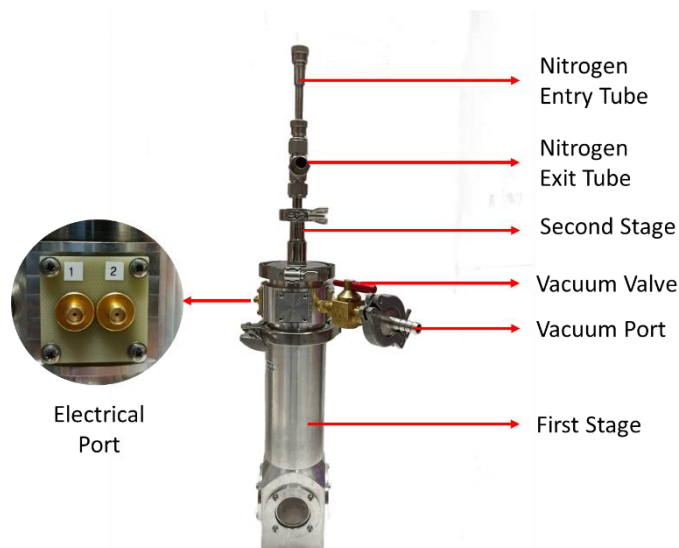


Figure 2.1 Parts of the Cryostat.

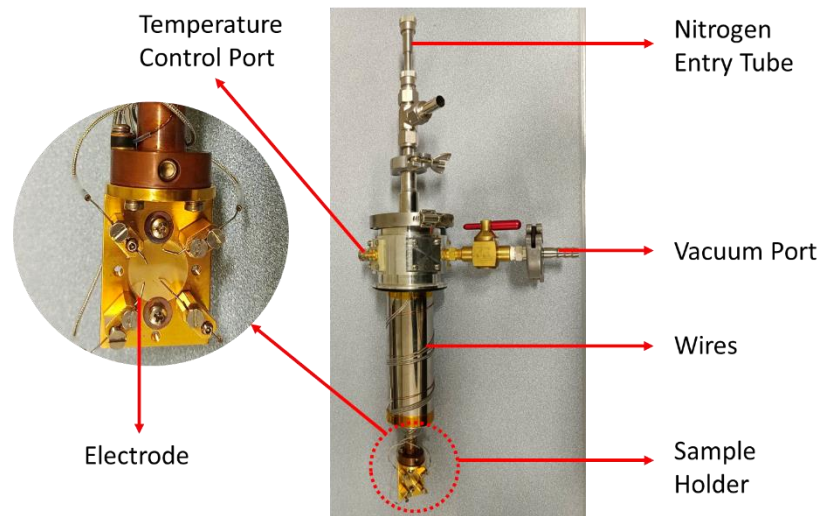


Figure 2.2 Inside view of Cryostat.

The second stage holds the sample, sensor and the heater to control the temperature inside the cryostat. A view of the second stage is provided in Fig. 2.2 where the inner structure can be observed. The inner part has a sample holder and four electrodes which are placed on the holder using screw and spring to keep a good mechanical contact at all temperatures. These 4 electrodes are connected with the electrical ports through wires and they can be used to contact the sample for transport and switching experiments.

Moreover, a sensor connected with the sample holder ensures a stable temperature between 78 K to 500 K by heating a resistor and a temperature controller (Lake Shore 336) can be connected to the cryostat using the temperature control port to stabilize the temperature in the cryostat. The stabilization is done by the PID controller and the value of expected temperature (setpoint), proportional (P), integral (I), and derivative (D) terms can be fixed using the buttons of the controller shown in Fig. 2.3. An external LabVIEW program can also be used to control these parameters.



Figure 2.3 Lake Shore 336 temperature controller.

Now, the aim is to connect the studied Mott material with this cryostat. For this purpose, the single crystal (GaMo_4S_8 and GaTa_4Se_8) are cleaved to obtain a clean and non oxidized surface for all the measurements. Then they are directly connected to the electrodes of the cryostat. This type of direct contact are stable at ambient temperature but it becomes unstable during cooling.

To eradicate the problem of stable connection, we developed a procedure by which the tiny crystals can be connected to the cryostat. The idea is to connect the sample with the substrate by a non-conductive glue and create an extended contact of large area on the substrate. The corresponding schematic is shown in Fig. 2.4 where two gold wires are used to connect the crystal with the extended contact by conductive glue. By this way, the electrode of the cryostat can be connected to the crystal via an extended contact and a reliable connection can be maintained.

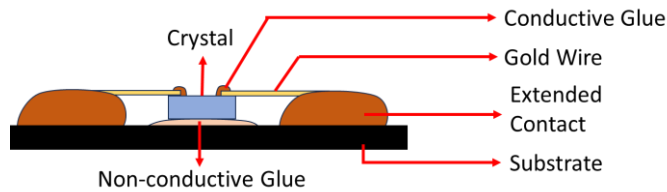


Figure 2.4 A Schematic showing crystal and the extended contact.

To do it practically, first the cleaved crystal is attached to the glass substrate using a nonconductive glue and heated in 120° C for 15 minutes. Then two gold wires having a diameter of 17.5 μm are connected to the sample using a conductive glue. The other sides of the gold wires are connected to a layer of conductive glue and it is again heated for 15 minutes in 120° C. After the heating the conductive glue solidifies and turns into an extended contact. A picture after the process is shown in Fig. 2.5.

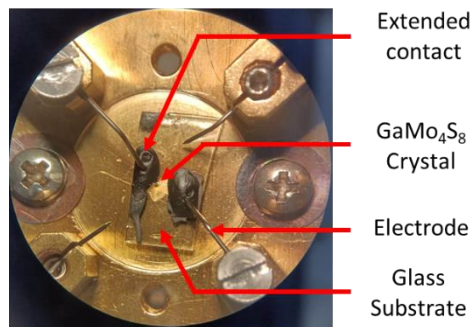


Figure 2.5 Crystal connected with the extended contact via gold wire.

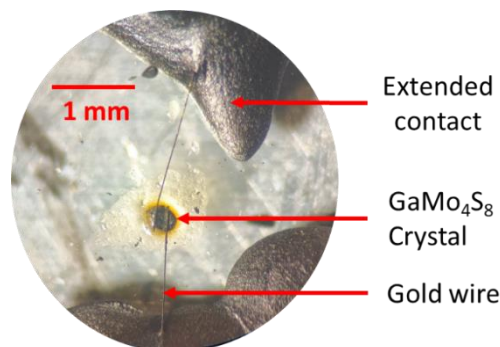


Figure 2.6 Electrodes are connected to a cleaved GaMo_4S_8 crystal through extended contact.

The advantage of using this type of configuration is that we do not connect the electrode of the cryostat directly to the sample but we connect it with the extended contact. Hence, the surface of the crystal is not destroyed by the slight movement of the electrode and a stable contact is ensured even when the temperature is varying. The Fig. 2.6 shows the configuration where the 2 electrodes of cryostat are connected with the GaMo_4S_8 crystal through the extended contact. Though using an extended contact adds some additional resistance but this is negligible compared to the sample resistance and it does not affect our measurement.

2.1.1 Setup for Transport Measurements

Now the studied Mott materials have been connected to the cryostat, it is time to discuss about the schematic of the cryogenic electrical setup for transport measurements. The circuit diagram for the transport measurement is provided in Fig. 2.7 where a DC current source (Yokogawa 7651) is used to provide a constant current signal in the sample and the voltage around the sample is observed by a voltmeter (Agilent 34401A). The sample is kept inside the cryostat and the temperature is varied for the transport measurement.

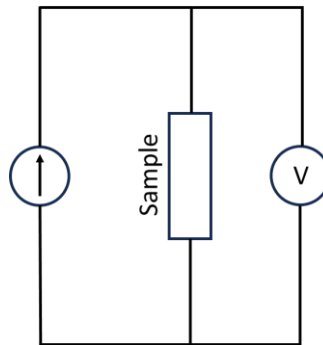


Figure 2.7 Circuit diagram for the transport measurements.

The resistance variation with temperatures using this cryogenic electrical setup is shown in Fig. 2.8. It can be observed from the figure that the resistance increases exponentially with decreasing temperature and a stable connection is obtained throughout this measurement. This proves the sustainability of our method to integrate small Mott crystals on the cryogenic electrical setup.

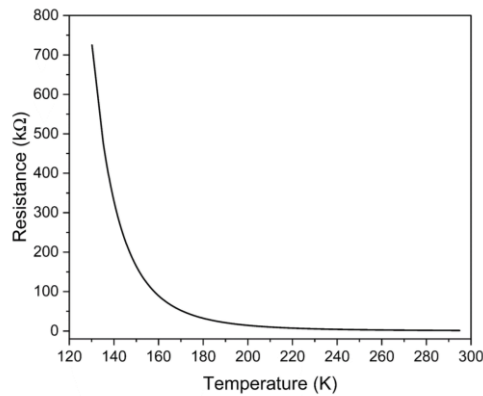


Figure 2.8 Resistance variation during the transport measurements.

2.1.2 Setup for Resistive Switching Measurements

The cryogenic electrical setup can be used for resistive switching measurements also. To observe the resistive switching phenomenon dynamically, an electric pulse generator is used to create the electric field in the sample and the time evolution of the sample resistance during the pulse is followed. The diagram for this measurement is shown in Fig. 2.9.

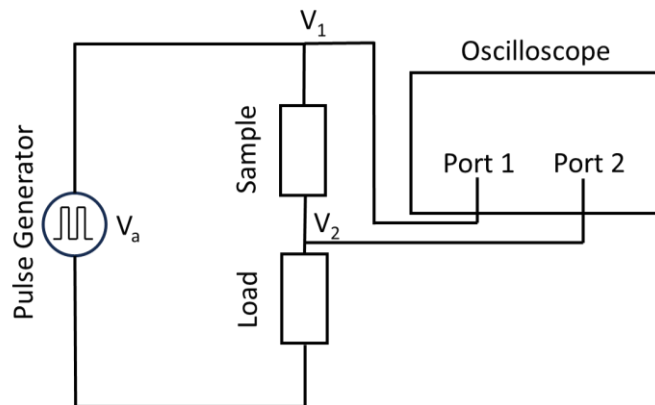


Figure 2.9 Circuit diagram for the resistive switching measurements.

To protect the sample from the overflow of current, a load resistance equal to 10% of the initial sample resistance is added with the sample in series. An oscilloscope (Rohde & Schwarz RTO 1002) is used to observe the voltage signal across the sample for the whole duration of input pulse. This is done by observing the two node voltages, V_1 and V_2 using the two port of the oscilloscope. Hence the sample voltage, V_s is the difference between these two node voltage.

$$V_s = V_1 - V_2 \quad (2.1)$$

As, the sample and load are in series, the same current flows through them. So, the current through the sample, I_s is expressed as:

$$I_s = \frac{V_2}{R_L} \quad (2.2)$$

Where, R_L is the load resistance. Thus finally the sample resistance, R_s can be calculated by:

$$R_s = \frac{V_s}{I_s} = \frac{V_1 - V_2}{I_s} \quad (2.3)$$

Thus using such setup allows us to observe the time evolution of the sample voltage and resistance during the whole period of the pulse.

2.2 Nanoprobe

The Omicron Nanoprobe system is a state of the art equipment that allow an electrical transport characterisation at the nanoscale. A nanoprobe system is composed of 4 scanning tunnelling microscope (STM) tips under a ultrahigh vacuum environment. The precise movement of electrodes (tips) is controlled through a piezoelectric elements and guided thanks to a coupled scanning electron microscopy (SEM). The tips can be either in tunnelling mode or in contact.

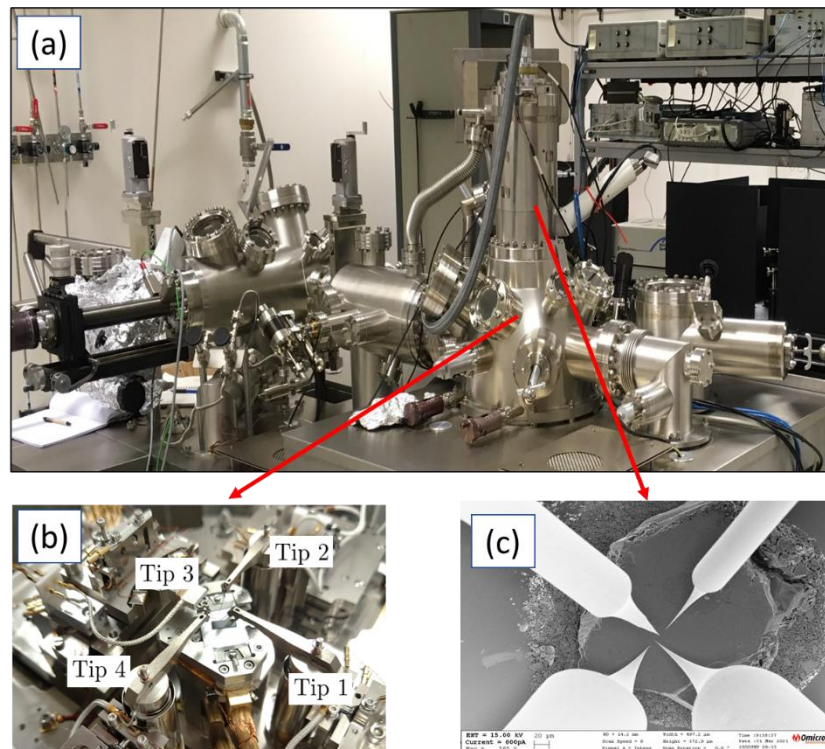


Figure 2.10 (a) Nanoprobe system; (b) Analysis chamber; (c) SEM image of 4 tips and sample.

A picture of the nanoprobe system is shown in Fig. 2.10(a). In this setup, the sample is transferred into analysis chamber through several vacuum chambers where 4 tips can be placed over the sample as shown in Fig. 2.10(b). A moving stage and control system allow the movement of both sample and the tips precisely which can be observed by the SEM images. The SEM image of the 4 tips and a GaMo_4S_8 sample is shown in Fig. 2.10(c). A SEM system uses an electron gun and lens to focus accelerated electrons on the sample. The accelerated electrons interact with the surface and secondary electrons are emitted from the atom. These secondary electrons have lower energies and they are created within few nanometres or below from the top surface [22]. Besides, the number of emitted secondary electrons depends on the topography of the sample. Hence, a detector system detects this varying number of secondary electrons and an image is constructed from this which represents the topography of the surface of the sample. The resolution of SEM is not limited by the diffraction limit but it is limited by the electron spot size. Hence, it provides satisfactory resolution to observe the topography of the sample and allow the electrode positioning.

2.3 Characterization technique

In this thesis, we are going to use conductive atomic force microscopy, energy-dispersive X-ray spectroscopy and Raman spectroscopy techniques to characterize the filament created by the non-volatile transitions. Hence, this section will be addressed to describe the principle of all these characterization techniques.

2.3.1 Conductive atomic force microscopy (C-AFM)

Atomic force microscopy is a characterization method that is used to observe the topography of any material at the nanoscale. It uses a probe which has a sharp tip on one side of the cantilever that is moved over the surface of the desired material. When the tip is brought near the surface of the material, the attraction force between the tip and the surface moves the tip closer. But as it gets closer, the repulsion force increases and it bends the cantilever as shown in Fig. 2.11. Then a laser beam is focused on the flat surface of the probe which is reflected from the top surface of it and is recorded by the positive-sensitive photodiode.

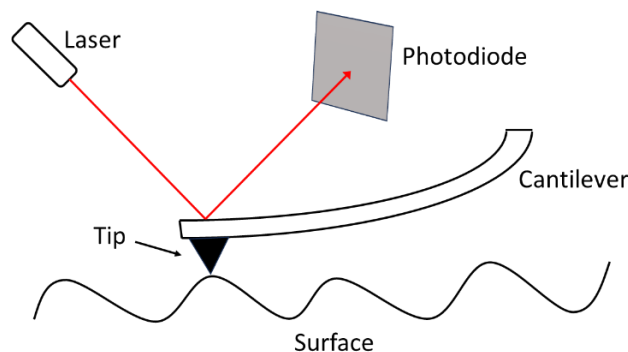


Figure 2.11 Schematic of AFM system (not to scale).

As the tip is moved over the surface of the sample, it is deflected differently depending on how much the surface is raised or lowered. The change of this deflection alters the direction of the reflected laser beam and the photodiode tracks and record this change. In this way, an accurate mapping of the surface topology can be obtained using the AFM.

The AFM can also be used to measure the conductivity of the surface (conductive AFM or C-AFM). In this case, a conductive tip is required and a fixed biasing voltage is applied into the cantilever. Besides, the sample is connected to the ground using a conductive line as shown in Fig. 2.12. By this way, the current through the sample is measured which gives a current image. So, in this mode, both topography and current image of the same sample area is generated. Noted that C-AFM is operated in contact mode where the repulsion forces between the tip and the surface dominates [23]. But the AFM can also be operated in tapping mode which we do not focus in this work.

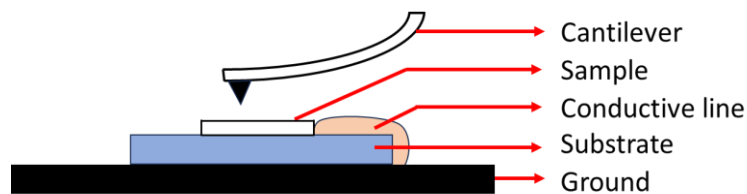


Figure 2.12 Schematic of AFM system (not to scale).

For the characterization in this work, Bruker Dimension 3100 AFM microscope with a PPP-CONTPT AFM probe will be used. The instrument is shown in Fig. 2.13. It has a head where the probe can be attached with the probe holder and the sample is placed over the stage which can be moved using a controller.

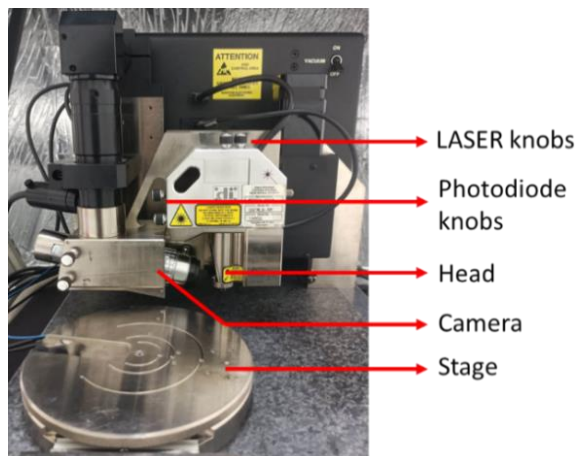


Figure 2.13 Bruker Dimension 3100 AFM microscope.

Before starting any measurement, the LASER is aligned on the cantilever using the LASER knobs and then the photodiode is aligned such that the reflected light can be detected by the photodiode. After this alignment procedure, the sample is brought under the head and the surface is focused with the camera. Finally, the tip is engaged on the area of interest at the surface of the sample and further measurements can be done.

2.3.2 Energy-dispersive X-ray spectroscopy (EDX)

Energy-dispersive X-ray spectroscopy commonly known as EDX is a characterization technique to analyse the chemical composition of the sample by collecting the characteristics x-ray emitted by the sample. When a high energy primary electron (PE) impinges on the sample, it knocks out an secondary electron (SE) from the inner shell (K shell) as shown if Fig. 2.14 (a) and then the electron from outer shell (M-shell) drops to lower shell to fill out the vacancy [24]. This causes a characteristic emission of x-ray from the sample as shown if Fig. 2.14 (b). Then this x-ray emission is detected by the detector for EDX analysis.

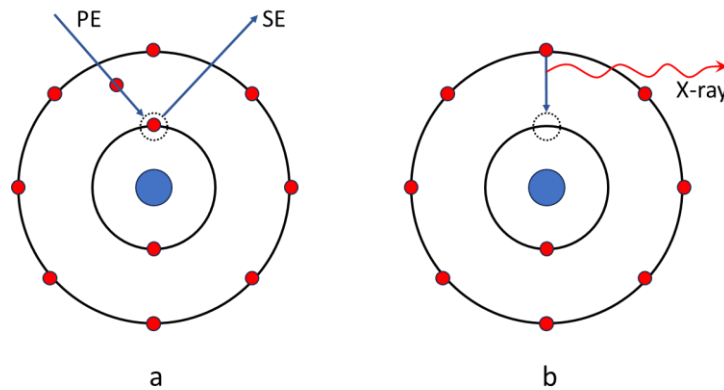


Figure 2.14 (a) Creation of SE; (b) Emission of x-ray.

In our measurement, we will use ZEISS Crossbeam 550 FIB-SEM device for SEM and EDX analysis. The accuracy of chemical analysis on this device can be improved by reducing the accelerating potential of the electron beam. Apart from this functions, this device can also be used for FIB (Focused Ion Beam), electron backscatter diffraction and electron beam lithography.

2.3.3 Raman Spectroscopy

Raman Spectroscopy relates to the inelastic scattering of light from the materials. This phenomenon was theoretically predicted by Smekal in 1923 and later experimentally observed by Raman and Krishnan in 1928. Generally, most of the photons that interacts with the molecule and scatters from it without causing any electronic transitions have the same energy as the incident photons. In this case, the molecule goes to a higher virtual state and returns back to its previous vibrational state. This process is an elastic scattering and known as the Rayleigh scattering. But very few photons go through an inelastic scattering and do not return to their previous vibrational states as shown in Fig. 2.15. In this situation, the scattered photon has a different energy compared to the incident photon and this is shown as Stokes and anti-Stokes shift which are used in Raman spectroscopy [25]. In room temperature, anti-Stokes processes are weak compared to the Stokes processes as the population in the higher vibrational state is less than the lower vibrational state.



Figure 2.15 Schematic of the Rayleigh and Raman processes.

In the Stokes process, the scattered photon contains less energy than the incident photon and this energy difference and the intensity is measured in Raman spectroscopy. In this spectroscopy, the shift in energy is expressed in terms of a wavenumber (cm^{-1}). As the wavenumber is proportional to the energy and also the energy of the incident photon is considered zero. Hence, the energy difference can be expressed in terms of the wavenumber and it doesn't depend on the frequency of the incident photon.

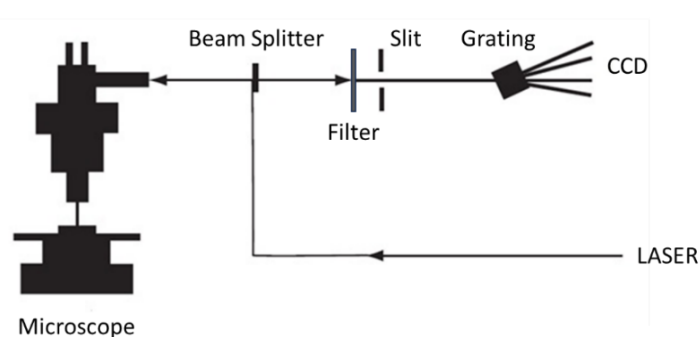


Figure 2.16 Diagram of Raman spectrometer [25].

The diagram of the Raman spectroscopy system is shown in Fig. 2.16. It consists of a microscope, a LASER, a grating, slits, a filter and a CCD detector. The sample is kept under the microscope and the interested area is focused which eradicates the influence of fluorescence. A visible LASER source is used and the beam is transmitted to the microscope through a beam splitter and it ensures the laser light to go towards microscope. Then the light is focused on the sample and the radiation is collected through the microscope and passed through a filter. The filter removes the photons having same frequency as the incident laser beam and thus only inelastically scattered photons are transmitted through it. Finally, using the grating they are divided into various frequency light and a CCD detector counts the number of photons incident on it. Thus, finally a spectrograph is obtained which shows the intensity with respect to the shifted energy.

Chapter 3 Volatile Transition

This chapter will focus on the electric field induced volatile transition of GaMo_4S_8 and GaTa_4Se_8 Mott materials. The term “volatile” means that the material returns back to its initial insulating state when the electric field is removed, by opposition to the so called “non-volatile” transition observed at higher electric field in narrow gap Mott insulators. We will start this chapter with the studied samples and characterization of the sample quality by the temperature dependent transport measurements at low electric field. Then we will focus our interest on the volatile switching phenomenon.

3.1 Studied Samples

The samples studied throughout this chapter are GaMo_4S_8 and GaTa_4Se_8 single crystals Mott materials. The crystals were prepared using the methods discussed in [26]. We are interested to study single crystals instead of deposited thin films to avoid any effect due to chemical contamination and disorder.

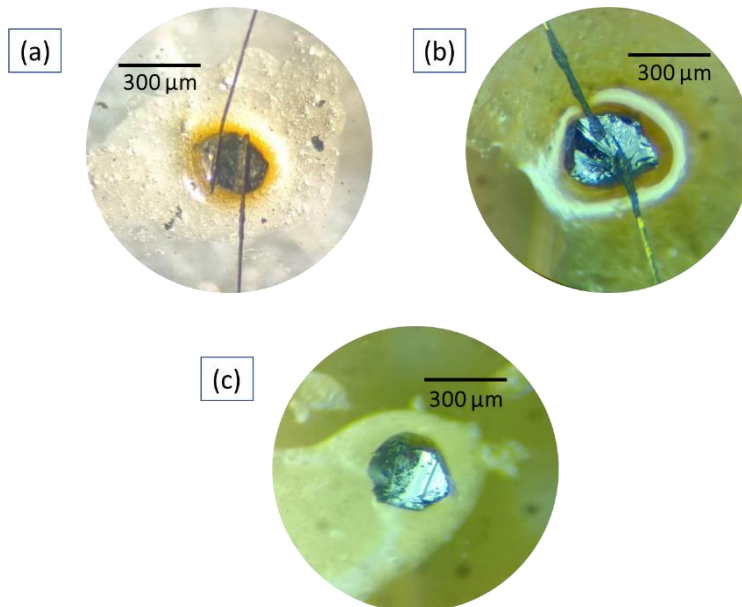


Figure 3.1 (a) GaMo_4S_8 sample 1; (b) GaMo_4S_8 sample 2; (c) GaTa_4Se_8 sample.

The crystals are cleaved and connected to the cryostat as explained in section 2.1 when it is used for the cryogenic electrical setup. The images of all the Mott crystals which will be studied in this chapter is shown in Fig. 3.1. The two GaMo_4S_8 crystals are shown in Fig. 3.1 (a-b) and these are addressed as GaMo_4S_8 sample 1 and 2 respectively. Finally, the GaTa_4Se_8 crystal is shown in Fig. 3.1 (c) and all these samples will be studied using the cryogenic electrical setup.

3.2 Transport Measurement at low electric field

In this measurement, our goal is to characterize the samples quality and determine the gap energy by measuring the temperature dependence of the sample resistance (at low electric field). For this, GaMo₄S₈ sample 1 and 2 will be used as Mott materials. The measurement is performed using the cryogenic electrical setup for transport measurements and the details about the setup have been previously discussed in section 2.1.1. First, the samples are connected with the cryostat and a fixed value of 1μA current is applied. Then by varying the temperature inside the cryostat, the evolution of sample resistance is obtained. The corresponding graph is shown in Fig. 3.2.

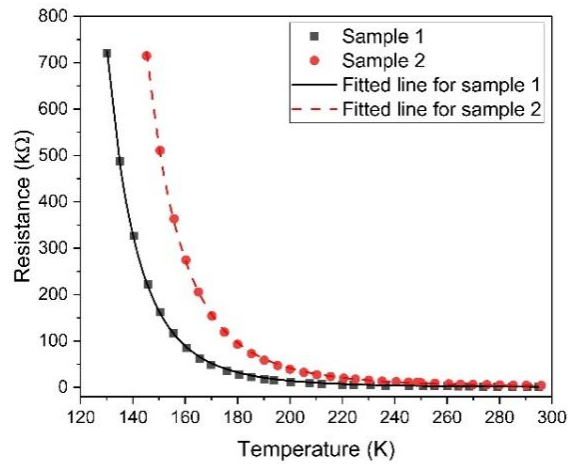


Figure 3.2 Resistance variation of GaMo₄S₈ sample 1 and 2 with temperature.

From this figure, we can observe that the resistance of both samples increase exponentially with decreasing temperature like a semiconductor. The resistance is fitted with the following equation which is used to express the temperature dependent resistance variation for a semiconductor:

$$R = R_0 \exp\left(\frac{E_g}{2K_b T}\right) \quad (3.1)$$

Where, E_g is the bandgap of the material, K_b is Boltzmann constant, T is the temperature and R_0 is a fitting parameter. After fitting, the bandgap is obtained and the results are summarized below:

GaMo ₄ S ₈	Sample 1	Sample 2	From Literature [4]
Bandgap (eV)	0.25	0.26	0.1-0.3

Table 3.1 Bandgap for the GaMo₄S₈ samples

From Table 3.1, it is clear that the experimental value lies within the range mentioned in the literature which proves that GaMo_4S_8 behaves like a low gap semiconductor. Moreover, the quality of the fit and the agreement with the tabulated bandgap indicate that the GaMo_4S_8 single crystals have a high purity and homogeneous stoichiometry.

3.3 Non-linear transport and electrical threshold

So far, it has been shown that the resistance varies depending on the temperature. But now the question arises “Does the resistance always remain constant at a given temperature?” To answer this question, we fix the temperature of the cryostat at 180 K and 200 K and vary the current source value to observe the voltage. The voltage versus current (VI) curve for GaMo_4S_8 sample 1 is shown in Fig. 3.3.

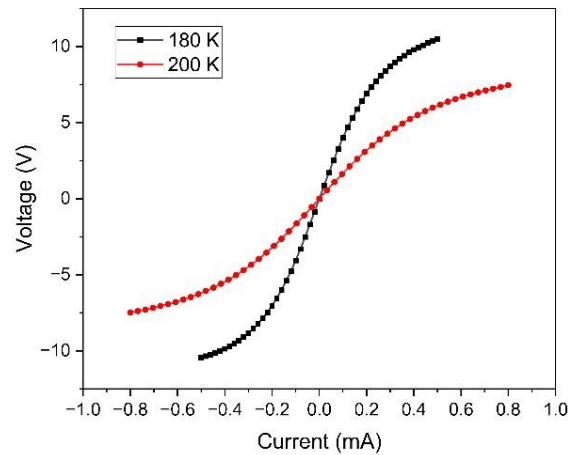


Figure 3.3 VI curve of GaMo_4S_8 sample 1 at 180 K and 200K.

From the Fig. 3.3, the following important things can be observed:

1. The graph has a linear and a non-linear region. The linear region shows an ohmic behaviour with a constant slope which means that the resistance of the sample is constant. But as the current through the sample is increased it enters the non-linear region and the slope decreases.
2. The voltage tends to be saturated as the current is increased. This saturation voltage represents the threshold voltage and it can be observed that the threshold voltage at 180 K is around 11 V. On the other hand, at 200 K the threshold voltage is around 7 V.

From this observation, it can be concluded that the resistance at a fixed temperature can be strongly reduced by applying more current through the sample and by reaching the threshold voltage. But what could be the reason behind it? The answer to this question will be discussed on the next section.

3.4 Switching & Delay Time

In the last section, we observed that the slope of the VI curve i.e. resistance at a particular temperature decreases at higher current value. When the current value is increased, the current density also increases. This eventually increases the electric field applied to the sample and when it goes above the threshold, the material goes through an IMT transition. So, the resistance of the sample abruptly reduced and we call it that the sample has been a switched.

To observe this switching phenomenon, the GaMo₄S₈ sample 2 is placed inside the resistive switching measurements setup discussed in section 2.1.2 and the temperature is kept fixed at 250 K. Then the pulse generator is used to generate a 30 V pulse ($V_a = 30$ V) with 5 ms duration. As the sample resistance at 250 K was 11.67 k Ω , so a of 470 Ω load resistance was added in series with it. The sample voltage evolution during the pulse duration is shown in Fig. 3.4 and it can be seen that the sample voltage drops to 11 V (threshold voltage). This means that the resistance of the sample has been decreased and which eventually caused the decrease of the sample voltage. Another important thing to be noticed here that the drop of voltage happens after a certain period of delay from the starting point of pulse. This time is called the delay time, t_d . Generally, the drop of voltage is not abrupt at lower electric field and till now, no hard and fast definition of the time delay has been mentioned in the literature. So, we define the time delay as the duration in which the sample voltage reaches 90 percent of its peak value. Throughout this report, we will use this definition to define the time delay. By using this definition, the time delay measured for the transition shown in Fig. 3.4 is found 1.17 ms.

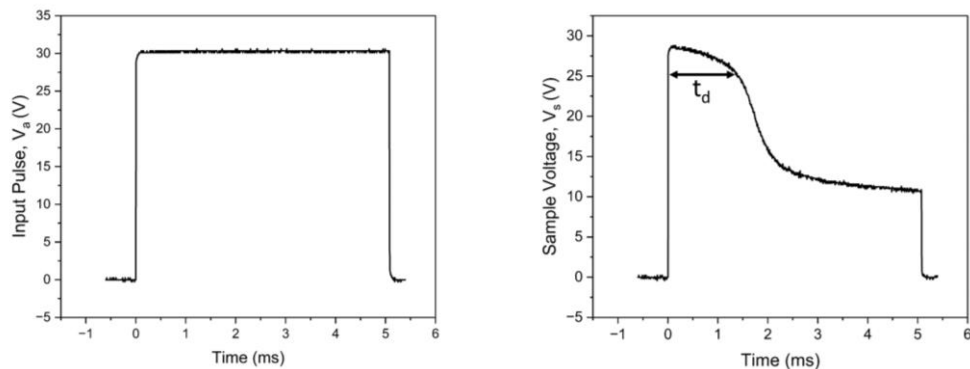


Figure 3.4 Resistive switching of GaMo₄S₈ sample 2 for 30 V input pulse (T=250 K).

Now, this time delay depends on the time of the formation of the filament between the electrodes which depends on the applied electric field. If the electric field is increased, the probability of the formation of the metallic site increases and less time is required for the formation of the filament. The sample voltage for various input pulses is shown in Fig. 3.5 which shows that the increasing value of input pulse reduces the delay time of transition which aligns with the literature found in [8][14].

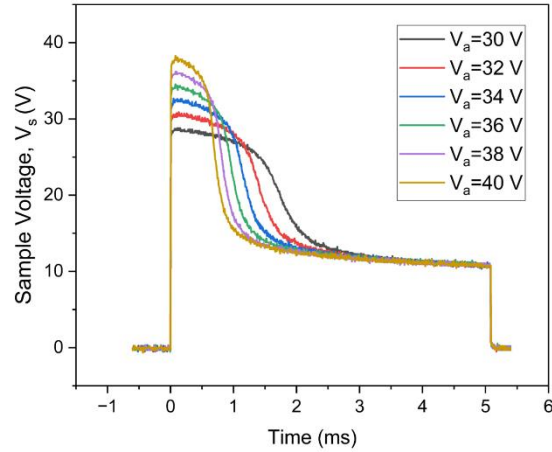


Figure 3.5 Sample voltage evolution for various input pulse for GaMo₄S₈ sample 2 (T=250 K).

Using the definition proposed in this report, we can extract the delay time from the sample voltage graph. The evolution of delay time with applied voltage pulse is shown in Fig. 3.6 and it shows that the delay time increases exponentially at lower electric field. It should be noted that the delay time near the threshold voltage (11 V) has not been determined. This is because at lower applied voltages, the filament formation becomes stochastic and the delay time cannot be deterministically measured. This property of Mott insulators has been recently reported by Rocco et al. [27] which explains the uncertainty of measuring the delay time near the threshold region.

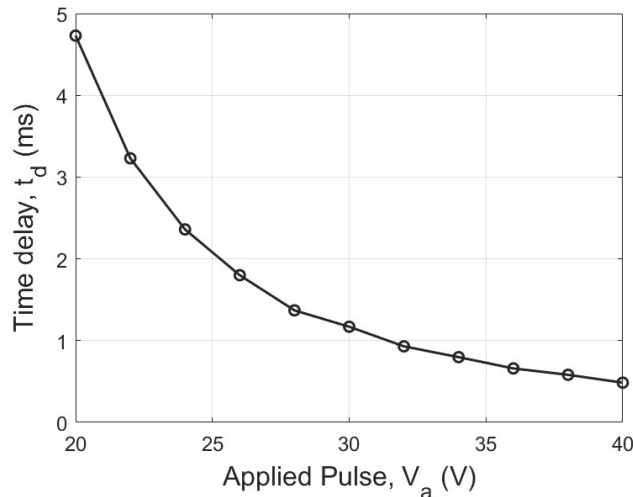


Figure 3.6 Delay time evolution with various input pulse for GaMo₄S₈ sample 2 (T=250 K).

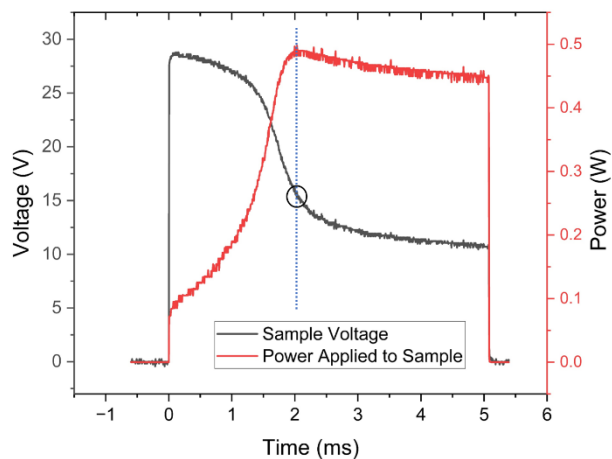
The delay time of GaMo₄S₈ sample 2 at 200 K, 250 K and 300 K have been summarised on Table 3.2. In all cases, the delay time decreases with increasing electric field as expected.

Applied Pulse (V)	Time Delay (ms) at 200 K	Time Delay (ms) at 250 K	Time Delay (ms) at 300 K
20	25.2	4.73	1.31
22	14.64	3.23	0.97
24	9.60	2.36	0.77
26	6.60	1.8	0.60
28	4.80	1.37	0.49
30	3.36	1.17	0.48
32	2.70	0.93	0.40
34	2.05	0.80	0.36
36	1.70	0.66	0.29
38	1.45	0.58	0.26
40	1.35	0.48	0.22

Table 3.2 Delay time evolution at 200 K, 250 K and 300 K for GaMo₄S₈ sample 2.

3.5 Switching Power and Energy

As seen on the previous section, the switching or delay time depends on the applied electric field. In order to evaluate the interest of such Mott material for the applications on electronic devices, it is necessary to determine the required switching power and energy. Lets consider that, a 30 V pulse of 5 ms duration is applied to the GaMo₄S₈ sample 2 at 250 K. In tis case, the corresponding voltage and applied power to the sample is shown in Fig. 3.7.

Figure 3.7 Sample voltage and power evolution for GaMo₄S₈ sample 2 (T=250 K).

It can be seen that the power reaches at maximum point at 2 ms, when the sample voltage drops to 15 V (marked by circle on the figure). This actually follows the maximum power transfer theorem. According to this theorem, highest power is delivered when the sample and load resistance becomes equal. In this case also, same thing is observed at 2 ms when the sample voltage and load resistance becomes equal and we observe half of the applied voltage (30 V) around the sample.

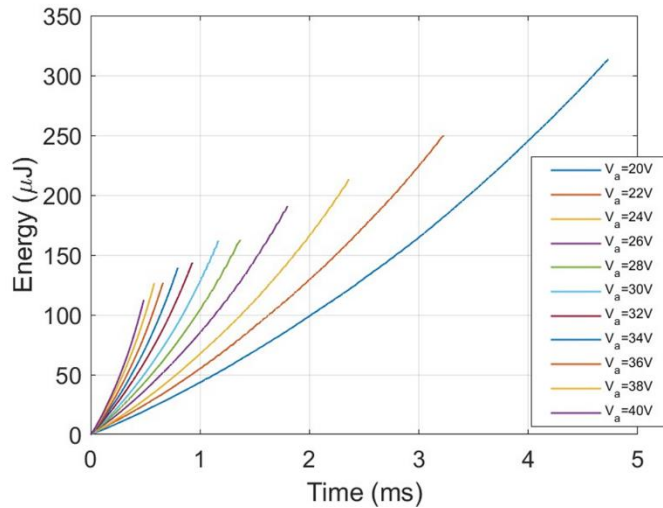


Figure 3.8 Evolution of switching power with delay time for GaMo₄S₈ sample 2 (T=250 K).

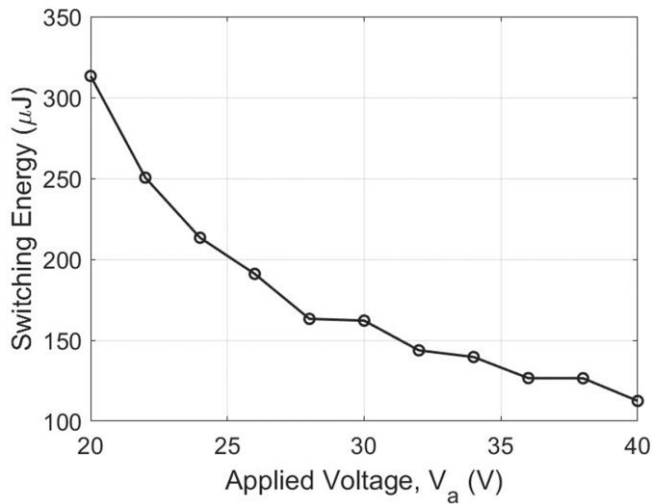


Figure 3.9 Switching power with applied voltage for GaMo₄S₈ sample 2 (T=250 K).

The switching energy value can be obtained by numerically integrating the Power graph from the starting point of the pulse till the switching point. By doing so, an evolution of energy with respect to the delay time can be obtained which is shown in Fig. 3.8. Clearly, at higher delay time values more energy is required for the switching. This can be better understood in Fig 3.9 where the switching energy is shown with respect to the applied pulse. At low applied voltage range (20 V -26 V),

switching energy increases because in this range the delay time exponentially increase with decreasing applied voltage. But at higher voltage region, the energy slightly decreases with some fluctuations with increasing applied voltage.

3.6 Modelling of Switching Phenomenon

The Mott transition is a first order transition, that are characterized by a characteristic specific heat. Hence, it can be assumed that there is a characteristic energy responsible for the transition and in this section we try to estimate it with a simple model.

According to this model, the electrons in the Mott material achieves power, P_w from the applied electric pulse which increases the energy of electron. This also enhances the electronic temperature T_e from the crystal temperature T_0 . Simultaneously, the electrons are also cooled down by a constant cooling power, P_c through the phonon electron interaction and the net energy difference between this two ongoing processes causes the breakdown (switching) in the material. This process is schematically shown in Fig. 3.10.

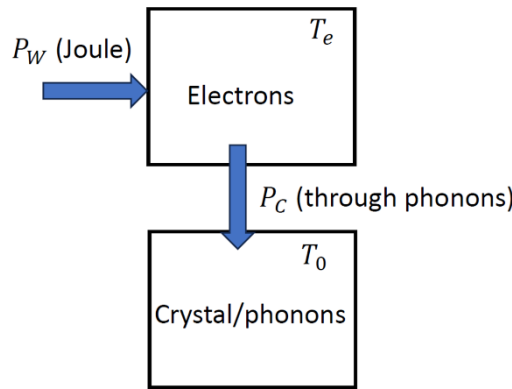


Figure 3.10 Schematic of the system.

The switching in the materials happens after a certain delay time. So, to calculate the net energy increase by the electron for switching we have to consider the power from the initial time up to delay time, t_d and it can be expressed as

$$\varepsilon = \int_0^{t_d} P_w dt - \int_0^{t_d} P_c dt \quad (3.2)$$

$$\varepsilon = \int_0^{t_d} \frac{V_s^2}{R_s} dt - \int_0^{t_d} P_c dt \quad (3.3)$$

Here, R_s is the resistance of the sample before transition and it is assumed to be constant. Thus the sample voltage, V_s also remains constant before switching. These assumptions are true when the applied voltages are two times or more higher than the threshold value.

Considering a constant cooling power, K_c and above assumptions we can rewrite equation 3.3 as

$$\varepsilon = \frac{V_s^2}{R_s} t_d - K_c t_d \quad (3.4)$$

This can further be rewritten as:

$$\frac{V_s^2}{R_s} = \varepsilon \frac{1}{t_d} + K_c \quad (3.5)$$

From this equation 3.5, it is observed that the applied power to the sample has a linear relationship with the inverse of time delay and the slope represents the characteristic energy for the transition.

Fig. 3.11 shows the experimental data obtained at 250 K and the corresponding fitted linear curve. Clearly, the experimental data points reveal a linear relationship between the applied power and the inverse of time delay.

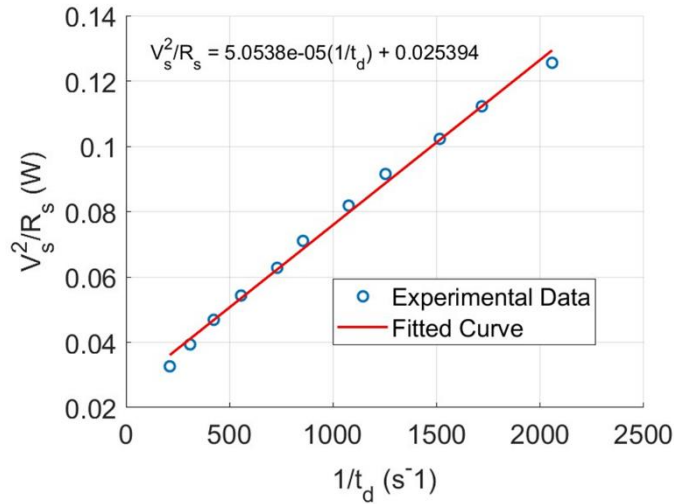


Figure 3.11 Linear fitting of applied power and inverse of time delay(T=250 K).

After fitting the experimental data, following linear equation is obtained:

$$\frac{V_s^2}{R_s} = 5.0538 \times 10^{-5} \frac{1}{t_d} + 0.025394 \quad (3.6)$$

Comparing equation 3.6 with equation 3.5, we obtain the energy of electrons, $\varepsilon = 5.0538 \times 10^{-5} \text{ J} = 50.54 \text{ } \mu\text{J}$ and cooling power 25.4 mW. The characteristic energy of the transition certainly depends on the volume of the studied sample on which the electric field is applied.

Here, we make a rough estimate by dividing the energy by the volume of the sample of about $200 \times 200 \times 50 \text{ } \mu\text{m}^3$ and obtain a characteristic energy per volume of around $25 \text{ pJ}/\mu\text{m}^3$. We can compare this value to the literature in other similar canonical Mott materials such as $(V_{1-x}Cr_x)_2O_3$ where 8 pJ energy was found for a sample of $1 \times 1 \times 0.2 \text{ } \mu\text{m}^3$ [28]. The energy values are quite different due to the difference of studied material and measurement temperature, so such study need to be continued.

Similar studies were also done at room temperature (300 K) and a characteristic energy of $57 \text{ } \mu\text{J}$ was obtained. Using the same sample volume estimation, the characteristic energy per volume is found $28 \text{ pJ}/\mu\text{m}^3$. But it is more difficult to conclude the characteristic energy at room temperature due to the thermal broadening effects.

3.7 Artificial Neuron

Artificial neuron is the main block of a neural network and AM_4Q_8 family materials can be used to implement an artificial neuron. This can be possible if a series of voltage pulse applied such that the on time duration of each pulse is less than delay time [1]. Hence, in this experiment, we use a stream of 10 pulse on $GaTa_4Se_8$ sample where each pulse has on time of 15 ms ($t_{on} = 15 \text{ ms}$) and off time of 5 ms ($t_{off} = 5 \text{ ms}$). The corresponding input pulse and the sample voltage is provided in Fig. 3.12 (b) and a transition i.e. drop of sample voltage can be observed on the 4th pulse. So, the material shows a cumulative effect and behaves like an integrator by integrating the input voltage.

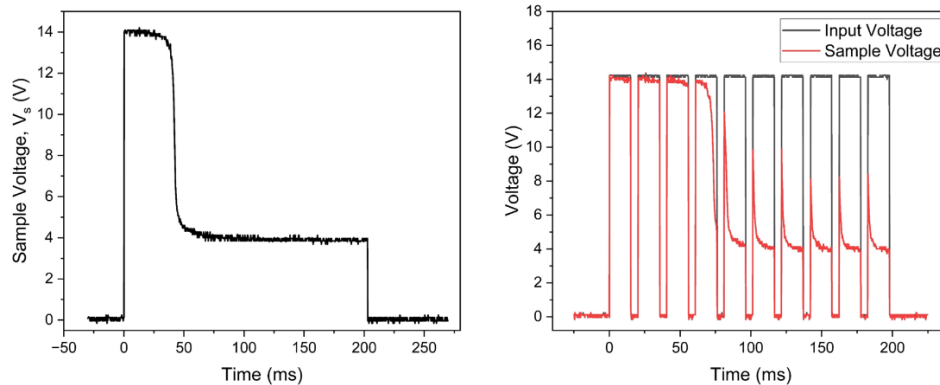


Figure 3.12 Switching on $GaTa_4Se_8$ sample at 78 K (a) 40 ms delay time observed for 14 V single pulse; (b) Neuronal effect observed for 14 V multi-pulse input.

Another thing to notice that the switching or firing time ($15 \times 4 = 60 \text{ ms}$) is higher than the delay time (40 ms) found for one applied pulse shown in Fig. 12 (a). This means that the integrator property of this material is not perfect and there are some leaky features during the off time. This happens due to the relaxation of metallic cells which means some metallic cells transforms back to insulating state. Thus, this material behaves as a leaky integrator.

The integrating behaviour can be well understood by observing the sample current during this multi-pulse experiment. As it is observed from Fig. 3.13 that very little current flows during the first 3 pulses but during the 4th pulse ($N_{\text{fire}}=4$), the neuron is fired. The number of pulses needed for the firing depends on the on and off time of input pulse. If the on time is increased, then the firing will occur at less number of pulses. But more pulses are required if the off time of input pulse is enlarged.

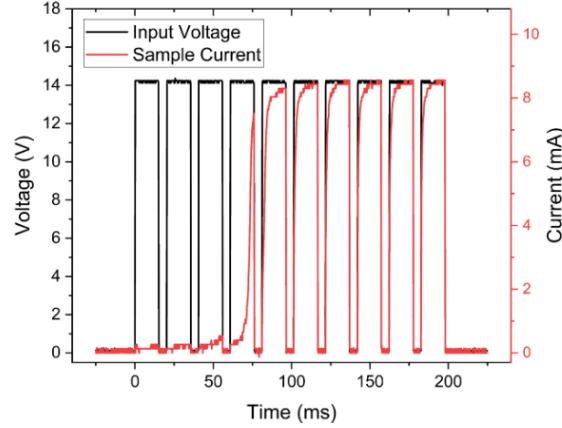


Figure 3.13 Neuronal effect on GaTa₄Se₈ sample at 78 K for 14 V multi-pulse

This behaviour is similar to a Leaky Integrate and Fire (LIF) model. In this model, the neuron is modelled as a parallel RC circuit where the capacitor voltage is analogous to the potential of the membrane of a biological neuron [29]. When the voltage in the capacitor exceeds the threshold value, an output signal is fired.

The voltage of the capacitor, V is expressed as [2]:

$$\frac{dV}{dt} = -V \frac{1}{RC} + \frac{w}{C} X(t) \quad (3.7)$$

Here, R is the leaky resistance, C is the membrane capacitance, w is the synaptic weight and $X(t)$ is the incoming signal to the neuron.

In contrary, the transition in a Mott insulator happens due to the dynamics of the number of metallic state cells, n_{CM} and it follows equation 1.6. When the applied voltage is greater than threshold, it can be written as [2]:

$$\frac{dn_{\text{CM}}}{dt} = -n_{\text{CM}} P_{\text{CM} \rightarrow \text{MI}} + A f(t) \quad (3.8)$$

Where, A is the production rate and $f(t)$ is a function whose value is 1 during the on time and 0 during the off time of applied pulse.

By comparing equation 3.7 and equation 3.8, a summary between the Mott neuron model and the LIF neuron model is provided in Table 3.3.

Item	Mott Neuron	LIF model
Variable	No. of metallic cells, n_{CM}	Membrane potential, V
Input	Voltage pulse	Dirac function
Output	Current signal	Not defined
Time constant	$1/P_{CM \rightarrow MI}$	RC

Table 3.3 Analogy between Mott neuron and LIF model.

This confirms that Mott insulators acts as a LIF neuron. Hence, this type of Mott insulators can be used to create a neural network.

Chapter 4 Filament Characterization

Generally, the resistive switching doesn't change the resistivity of the whole material but creates a low resistive filament region between the electrodes which dominates the electrical transport. So, it is important to know the geometry, conductivity, chemical composition to realize its application on a device. This chapter is addressed to induce a NV resistive switching and to characterize the properties of the metallic filament at the nanoscale. The obtention of the NV resistive switching was however made difficult by the setup limitation in terms of voltage and temperature : according to the literature, a voltage of 5 times the threshold voltage is necessary to induce the non-volatile resistive switching. Moreover, the temperature must be low enough to limit the amount of thermal carriers and avoid undesired effects due to Joule heating. The first part will be focused on a specific non reversible resistive change obtained at the surface of the studied sample using the Nanoprobe. Later parts of this chapter will be focused on the filament characterization by C-AFM, EDX and Raman spectroscopy techniques to know about the topography, conductance and chemical composition of the filament. Throughout this chapter, GaMo_4S_8 sample 3 will be studied. An SEM image of the studied sample is provided in Fig. 4.1.

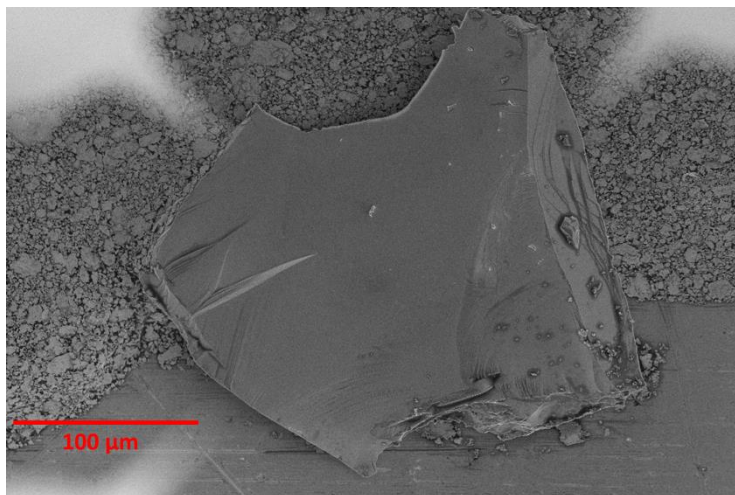


Figure 4.1 SEM image on the GaMo_4S_8 sample 3 (studied sample)

4.1 Filament Creation

In the last chapter, the resistive switching was done by means of a temporary filament creation between the electrodes. But now the goal is to create a permanent filament between the electrodes and this can be done by applying a high electric field into the sample.

The studied sample was transferred inside the analysis chamber of the nanoprobe and tungsten tips were used as the contact electrode. By using the moving stage and control system, these tips were used to create filament as shown in Fig. 4.2. The sample transfer inside the chamber and the filament creation was performed by the PhD student, Houda Koussir.

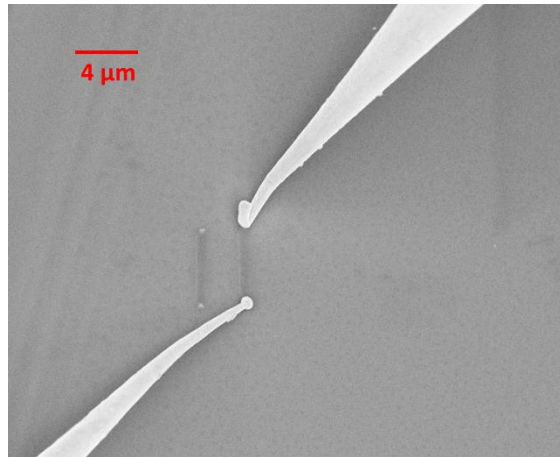


Figure 4.2 SEM image on the GaMo₄S₈ sample 3 showing filament creation by 2 tips

Multiple filaments on the surface of the crystal can be created and this allow us to create a pattern “IEMN” on the surface. The corresponding SEM image is shown in Fig. 4.3. For each filament formation, the interelectrode distance was between 4.5 μm – 5 μm and 16 V – 20 V were applied through the tips.

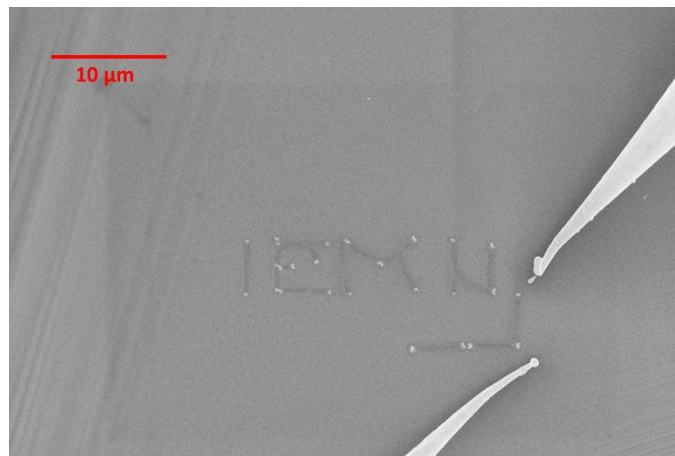


Figure 4.3 SEM image on the GaMo₄S₈ sample 3 showing the pattern IEMN.

Generally Mott non-volatile filaments creation require around 5 times of the threshold voltage and are reversible. But these filaments were created using 20 V when the threshold voltage was 12 V. Additionally, the filaments were irreversible and the resistances was measured with the nanoprobe, and a systematic decrease by a factor 50 is observed. To analyse the origin of such change, the sample has been characterized by the C-AFM, EDX and Raman spectroscopy.

4.2 C-AFM characterization

C-AFM is a probe based characterization technique where the probe is contacted with the sample to observe the topography and local conductivity of the sample. Some observations on the topography and conductance of the filament due to resistive switching device have been done proving the effectiveness of this characterization technique at nanoscale [30][31]. Moreover, C-AFM has also been used by Babich et al. to observe a buried conductive filament induced by a non volatile Mott resistive switching in $(V_{0.95}Cr_{0.05})_2O_3$ [32]. Motivating from these works, the same technique will be applied to study the filament of two different samples created using cryostat and nanoprobe respectively.

We first focus on the topography of the filaments created on $GaMo_4S_8$ sample 3 by the nanoprobe. The pattern consists of multiple filaments which were created sequentially. The AFM images of the topography of the sample showing the pattern "IEMN" is presented in Fig. 4.4 (a-c) where the patterns can be easily observed. Fig. 4.4 (d) shows the zoomed view of one particular filament of the pattern.

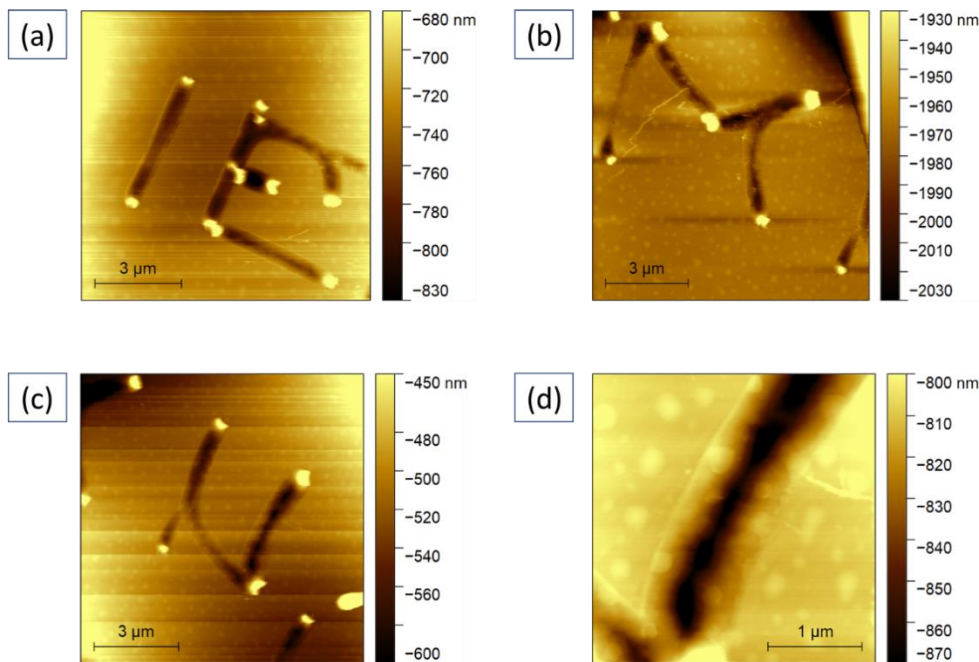


Figure 4.4 AFM image of the $GaMo_4S_8$ sample 3 (a-c) showing different alphabets of the pattern created on the sample; (b) zoomed view of a particular filament.

Now to observe more details about the shape of the filament it is necessary to extract the width and depth of the filament. This can be possible by extracting the profile along some arbitrary directions chosen from the AFM images. To do so, four arbitrary lines have been drawn and the corresponding image is shown in Fig. 4.5.

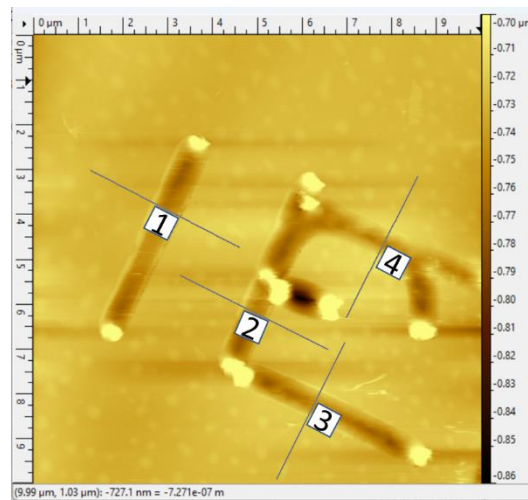


Figure 4.5 Arbitrary lines drawn on the AFM image shown in Fig. 4.4 (a).

The profile along these 4 lines are extracted by using the Gwyddion software. The profile is shown in Fig. 4.6 and it can be observed that the width and depth profile for filaments are almost uniform. The profile shows an average filament width of 700 nm and an average depth of 40 nm. This provides a depth width ratio of 5%.

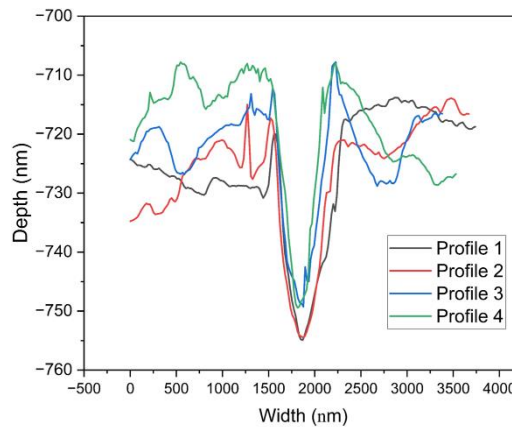


Figure 4.6 Depth and Width profile of the image shown in Fig. 4.5.

Now, focusing on the conductivity map of the pattern it can be observed that the filaments are more conductive than the outside pristine areas which can be seen from Fig. 4.7 (a-c). To have a more better view, one single filament of the pattern has been observed in Fig. 4.7 (d). A close observation on this figure shows that the edges of the filament are much more conductive compared to the inner areas of the filament.

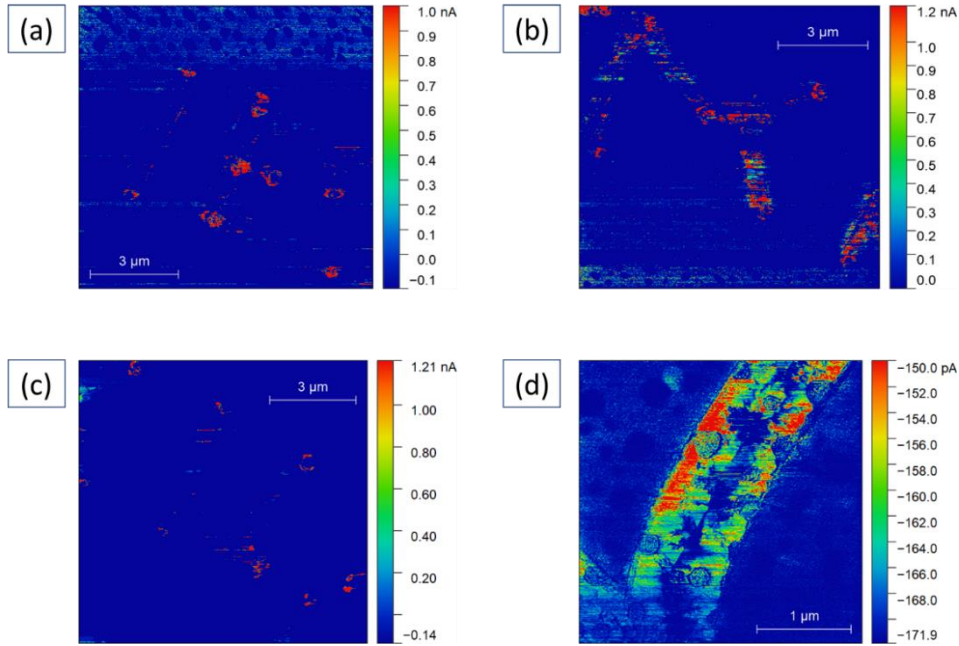


Figure 4.7 Conductance map of the GaMo₄S₈ sample 3 (a-c) showing conductance of the pattern created on the sample; (b) zoomed view of a particular filament.

An overlaid view of the conductance map with the topography of a single filament shown in Fig. 4.8 further confirms this observation. From this figure, it can be seen that the edges of filaments has higher conductivity compared to the pristine areas. Moreover, the conductance on the filament appears to be non-uniform. There seems to be a difference in conductance between the edges and the inner region of the filament. This happened due to a bad contact between the tip and the sample during the scanning time because of the topography of the filament.

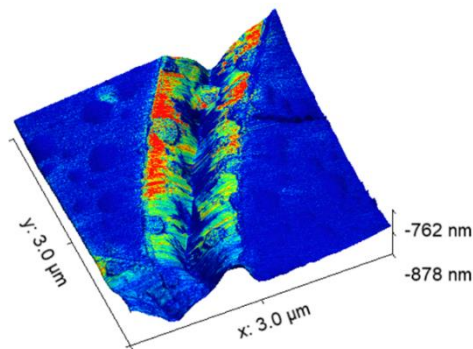


Figure 4.8 Overlaid image of conductance map and topography of a filament of the GaMo₄S₈ sample 3

In summary, the filaments created by using the nanoprobe shows trench topography and appears to be more conductive than the pristine areas. This concludes that a trench shaped conductive filament can be created between the electrodes by applying an electric field.

4.3 EDX characterization

In order to perform the chemical characterization, three areas are chosen on the studied sample as shown in Fig. 4.9. Here, Area 1 is the pristine area where no transitions have been done. On the other hand, area 2 and 3 are chosen inside the filament and they are conductive than area 1. The speciality about area 3 is that it has gone through some kind of changes during the C-AFM characterization. This happened accidentally because of a higher biasing on the AFM. Hence, this area is also interesting to be studied because it will also unveil the effect of an AFM tip biasing on the sample.

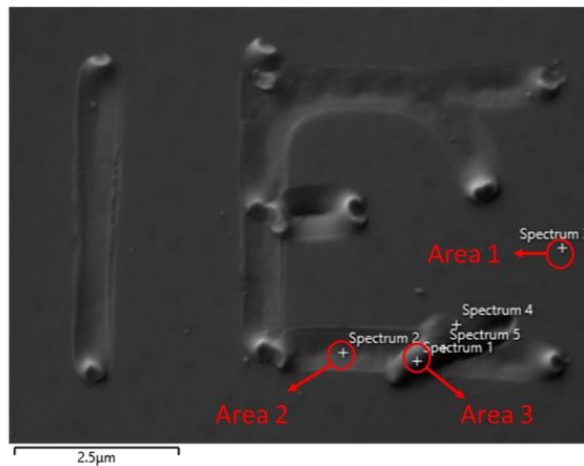


Figure 4.9 Areas chosen for EDX characterization on GaMo₄S₈ sample 3.

The EDX measurement graph of area1 is presented in Fig. 4.10. By observing the peak, it can be said that the material is composed of Ga, Mo and S. The peak of impurity carbon arises from the presence of glue.

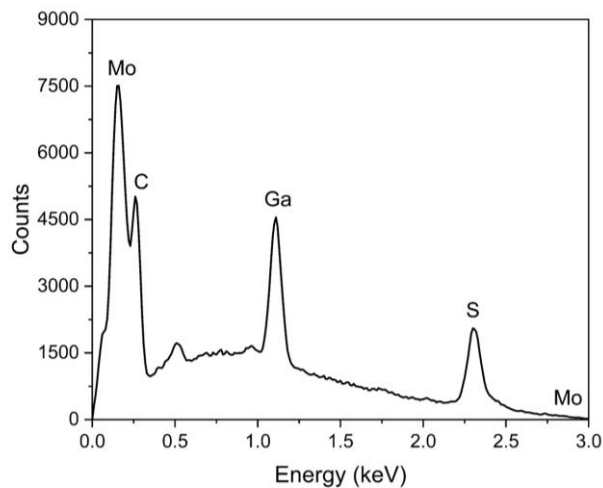


Figure 4.10 EDX spectra of area 1 on GaMo₄S₈ sample 3.

On the other hand, area 2 shows additional peaks of W along with Ga, Mo and S that have come from the electrode of the nanoprobe. Besides, it can be observed that the peak of Ga decreased compared to the spectra provided in Fig. 4.11. This arises a doubt that the filament may be chemically changed compared to the pristine areas.

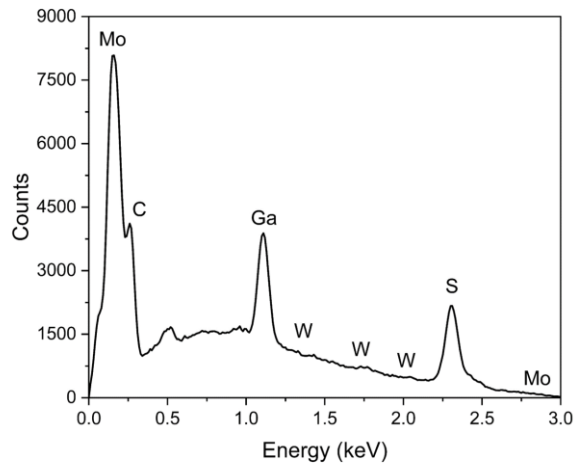


Figure 4.11 EDX spectra of area 2 on GaMo_4S_8 sample 3.

Interestingly, area 3 also shows different spectra than area 2 shown in Fig. 4.12. It shows an additional composition of Oxygen along with Ga, Mo and W. The presence of oxygen ensures that the filament goes through some chemical reaction with the oxygen of the air in presence of a higher biasing voltage on the AFM tip. Because of the higher contact resistance between the AFM tip and the sample, a biasing voltage creates high temperature which initiates a chemical reaction among the elements present on the filament and the oxygen in the air.

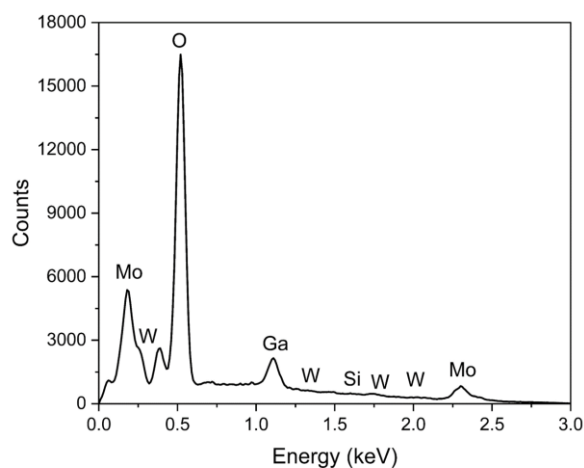


Figure 4.12 EDX spectra of area 3 on GaMo_4S_8 sample 3

The quantity of the elements observed in area 1, 2 and 3 measured in weight ratio percentage is listed in Table 4.1 which shows the increase of Mo and decrease of Ga in the filament. This proves that the filament has been subject to a chemical transition.

Elements	Area 1 (Weight %)	Area 2 (Weight %)	Area 3 (Weight %)
Ga	6.57	5.00	3.80
Mo	56.45	59.67	77.21
S	33.28	31.91	N/A
C	3.70	2.68	N/A
W	N/A	0.73	0.14
O	N/A	N/A	18.37
Si	N/A	N/A	0.49

Table 4.1 EDX weight ratio of 3 areas on GaMo₄S₈ sample 3.

4.3 Raman characterization

In the last section, it was observed that the filament has been chemically changed but now the aim is to further confirm it through Raman characterization on GaMo₄S₈ sample 3. This technique acts as a fingerprint of the material and by observing the peaks the material can be detected.

First the Raman spectrum is observed at the pristine area which is presented in 4.13. This figure shows a lot of peaks corresponding the various bonds and complex structure present in the GaMo₄S₈ material.

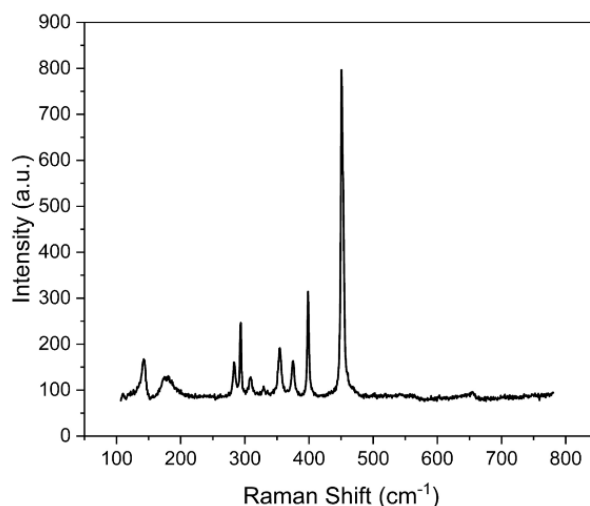


Figure 4.13 Raman shift of GaMo₄S₈ sample 3 on pristine area.

But the Raman spectra of the filament area shown in Fig. 4.14 reveal 3 peaks positioned at 381 cm^{-1} , 407 cm^{-1} and 450 cm^{-1} respectively. This is similar to the Raman shift found in MoS_2 materials where two characteristic peak appears near 385 cm^{-1} (E_{2g}) and 404 cm^{-1} (A_{1g}) for single layer MoS_2 [33]. These characteristic positions are sensitive to the number of layer and the distance between these two bands increases with increasing number of layers. On the other hand, the peak around 450 cm^{-1} is due to the double resonant second-order Raman processes and it is not sensitive on the number of layers but varies depending on the substrate [34].

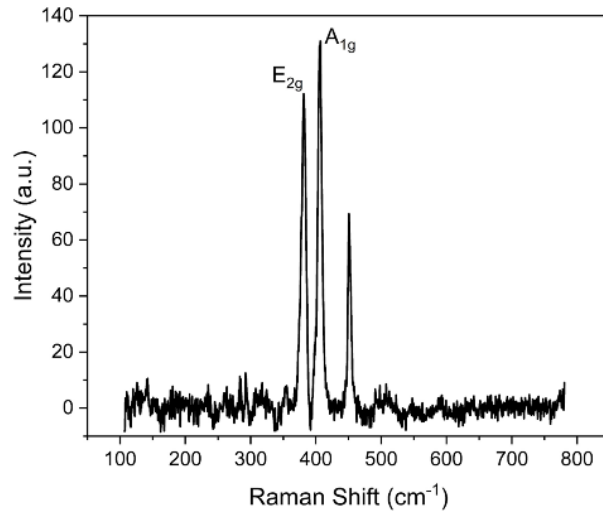


Figure 4.14 Raman shift of GaMo_4S_8 sample 3 on the filament.

So it has been confirmed that the filament is composed of MoS_2 materials and to know more about the nature, the zoomed view of Raman shift near E_{2g} and A_{1g} bands are provided in Fig. 4.15.

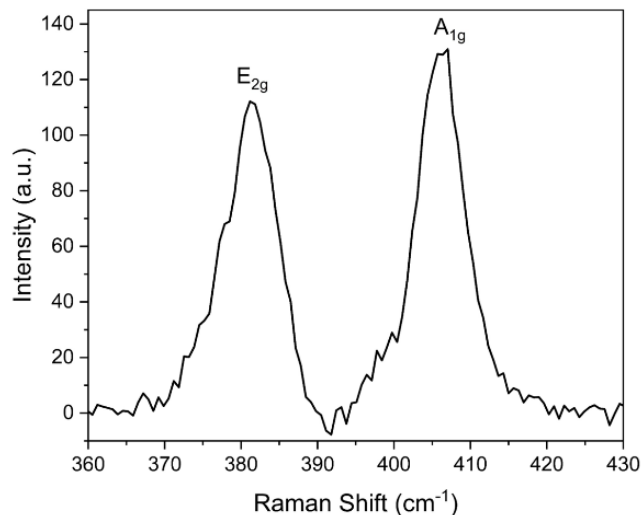


Figure 4.15 Raman shift of GaMo_4S_8 sample 3 on the filament showing E_{2g} and A_{1g} bands.

It is found from the literature that the peak of E_{2g} band is blue shifted from 381 cm^{-1} and the A_{1g} is red shifted from 404 cm^{-1} as the number of layers are increased. Moreover, for a bulk MoS_2 material, the peaks have been founded in 381.5 cm^{-1} and 406.6 cm^{-1} respectively [33]. On the studied sample, the peak of E_{2g} band and A_{1g} band appeared at 381 cm^{-1} and 407 cm^{-1} respectively. These observed value coincides with the value found for bulk MoS_2 material and hence it can be concluded that the filament formation observed after application of short voltage pulses at the surface of GaMo_4S_8 is a chemical change from a crystalline GaMo_4S_8 to a crystalline bulk MoS_2 bulk filament.

Conclusions & Future Work

AM4Q₈ family of Mott material is interesting due to its potential application in the electronic devices as a memory and artificial neuron. These applications are possible through the IMT transition done by electric field which creates a conductive filament. From the application point of view, the switching energy is a critical parameter and in this master internship report, this issue is addressed. By adapting the cryogenic electrical setup for single crystal Mott insulator and performing the switching measurement, It was found that switching energy varies between 313 μJ and 112 μJ depending on the applied pulse at 250 K. As the transitions are of first order, a simple model was introduced and a characteristic energy of 25 $\text{pJ}/\mu\text{m}^3$ was found during this transition at 250 K. Besides, the neuronal behaviour of this material was compared with the LIF model.

The latter part of the report was dedicated characterization of to the filament created by the small electric field. It was observed that the filament created by small electric field creates conductive and trench shaped filament, but it does not correspond to the Mott transition. This was primarily confirmed by the EDX analysis showing a higher Mo and less Ga weight ratio on the filament compared to the pristine area. Later, It was further confirmed through the Raman characterization where the filament showed characteristics peak at 381 cm^{-1} and 407 cm^{-1} . This enabled us to confirm that the filament is made of MoS₂ which concludes that the filament created by small electric field corresponds to a specific irreversible transition.

Though a hypothetical model was introduced to explain the switching energy but further works are needed to correlate the switching energy with the sample volume. This will lead to the realization of such Mott materials for switching applications. In addition, modelling the Mott neuron is a future work to explore as it may be used to implement a hardware neural network which will open a new perspective of Mott materials in neuromorphic computing.

References

- (1) Adda, C.; Tranchant, J.; Stoliar, P.; Corraze, B.; Janod, E.; Gay, R.; Llopis, R.; Besland, M. P.; Hueso, L. E.; Cario, L. An Artificial Neuron Founded on Resistive Switching of Mott Insulators. 2017 IEEE 9th Int. Mem. Work. IMW 2017 2017, 8–11. DOI: 10.1109/IMW.2017.7939071.
- (2) Stoliar, P.; Tranchant, J.; Corraze, B.; Janod, E.; Besland, M. P.; Tesler, F.; Rozenberg, M.; Cario, L. A Leaky-Integrate-and-Fire Neuron Analog Realized with a Mott Insulator. *Adv. Funct. Mater.* 2017, 27 (11), 1–7. DOI: 10.1002/adfm.201604740.
- (3) Oh, S.; Shi, Y.; del Valle, J.; Salev, P.; Lu, Y.; Huang, Z.; Kalcheim, Y.; Schuller, I. K.; Kuzum, D. Energy-Efficient Mott Activation Neuron for Full-Hardware Implementation of Neural Networks. *Nat. Nanotechnol.* 2021, 16 (6), 680–687. DOI: 10.1038/s41565-021-00874-8.
- (4) Janod, E.; Tranchant, J.; Corraze, B.; Querré, M.; Stoliar, P.; Rozenberg, M.; Cren, T.; Roditchev, D.; Phuoc, V. T.; Besland, M. P.; Cario, L. Resistive Switching in Mott Insulators and Correlated Systems. *Adv. Funct. Mater.* 2015, 25 (40), 6287–6305. DOI: 10.1002/adfm.201500823.
- (5) Tranchant, J.; Janod, E.; Corraze, B.; Stoliar, P.; Rozenberg, M.; Besland, M. P.; Cario, L. Control of Resistive Switching in AM4Q8 Narrow Gap Mott Insulators: A First Step towards Neuromorphic Applications. *Phys. Status Solidi Appl. Mater. Sci.* 2015, 212 (2), 239–244. DOI: 10.1002/pssa.201400158.
- (6) del Valle, J.; Salev, P.; Kalcheim, Y.; Schuller, I. K. A Caloritronics-Based Mott Neuristor. *Sci. Rep.* 2020, 10 (1), 1–10. DOI: 10.1038/s41598-020-61176-y.
- (7) Correlations, E.; Energy, N.; Author, B.; Source, H.; Royal, T.; Stable, S. Electron Correlations in Narrow Energy Bands. *Proc. R. Soc. London. Ser. A. Math. Phys. Sci.* 1963, 276 (1365), 238–257. DOI: 10.1098/rspa.1963.0204.
- (8) Guiot, V.; Cario, L.; Janod, E.; Corraze, B.; Ta Phuoc, V.; Rozenberg, M.; Stoliar, P.; Cren, T.; Roditchev, D. Avalanche Breakdown in GaTa₄Se₈-XTex Narrow-Gap Mott Insulators. *Nat. Commun.* 2013, 4 (1), 1722. DOI: 10.1038/ncomms2735.
- (9) Vaju, C.; Cario, L.; Corraze, B.; Janod, E.; Dubost, V.; Cren, T.; Roditchev, D.; Braithwaite, D.; Chauvet, O. Electric-Pulse-Induced Resistive Switching and Possible Superconductivity in the Mott Insulator GaTa₄Se₈. *Microelectron. Eng.* 2008, 85 (12), 2430–2433. DOI: 10.1016/j.mee.2008.09.026.
- (10) Pocha, R.; Johrendt, D.; Ni, B.; Abd-Elmeguid, M. M. Crystal Structures, Electronic Properties, and Pressure-Induced Superconductivity of the Tetrahedral Cluster Compounds GaNb₄S₈, GaNb₄Se₈, and GaTa₄Se₈. *J. Am. Chem. Soc.* 2005, 127 (24), 8732–8740. DOI: 10.1021/ja050243x.

- (11) Ta Phuoc, V.; Vaju, C.; Corraze, B.; Sopracase, R.; Perucchi, A.; Marini, C.; Postorino, P.; Chligui, M.; Lupi, S.; Janod, E.; Cario, L. Optical Conductivity Measurements of GaTa₄Se₈ under High Pressure: Evidence of a Bandwidth-Controlled Insulator-to-Metal Mott Transition. *Phys. Rev. Lett.* 2013, 110 (3), 1–5. DOI: 10.1103/PhysRevLett.110.037401.
- (12) Camjayi, A.; Acha, C.; Weht, R.; Rodríguez, M. G.; Corraze, B.; Janod, E.; Cario, L.; Rozenberg, M. J. First-Order Insulator-to-Metal Mott Transition in the Paramagnetic 3D System GaTa₄Se₈. *Phys. Rev. Lett.* 2014, 113 (8), 1–5. DOI: 10.1103/PhysRevLett.113.086404.
- (13) Park, M. J.; Sim, G. B.; Jeong, M. Y.; Mishra, A.; Han, M. J.; Lee, S. Bin. Pressure-Induced Topological Superconductivity in the Spin–Orbit Mott Insulator GaTa₄Se₈. *npj Quantum Mater.* 2020, 5 (1), 1–6. DOI: 10.1038/s41535-020-0246-0.
- (14) Diener, P.; Janod, E.; Corraze, B.; Querré, M.; Adda, C.; Guilloux-Viry, M.; Cordier, S.; Camjayi, A.; Rozenberg, M.; Besland, M. P.; Cario, L. How a Dc Electric Field Drives Mott Insulators out of Equilibrium. *Phys. Rev. Lett.* 2018, 121 (1), 19–22. DOI: 10.1103/PhysRevLett.121.016601.
- (15) Stoliar, P.; Cario, L.; Janod, E.; Corraze, B.; Guillot-deudon, C.; Salmonbourmand, S.; Guiot, V.; Tranchant, J.; Rozenberg, M. Universal Electric-Field-Driven Resistive Transition in Narrow-Gap Mott Insulators. *Adv. Mater.* 2013, 25 (23), 3222–3226. DOI: 10.1002/adma.201301113.
- (16) Tesler, F.; Adda, C.; Tranchant, J.; Corraze, B.; Janod, E.; Cario, L.; Stoliar, P.; Rozenberg, M. Relaxation of a Spiking Mott Artificial Neuron. *Phys. Rev. Appl.* 2018, 10 (5), 1. DOI: 10.1103/PhysRevApplied.10.054001.
- (17) Souchier, E.; Cario, L.; Corraze, B.; Estournes, C.; Fernandez, V.; Skotnicki, T.; Mazoyer, P.; Janod, E.; Besland, M.-P. Thin Layers Obtained by Plasma Process for Emerging Non-Volatile Memory (RRAM) Applications. In 2009 IEEE International Memory Workshop 2009. 1–2. DOI: 10.1109/IMW.2009.5090608.
- (18) Corraze, B.; Janod, E.; Cario, L.; Moreau, P.; Lajaunie, L.; Stoliar, P.; Guiot, V.; Dubost, V.; Tranchant, J.; Salmon, S.; Besland, M. P.; Phuoc, V. T.; Cren, T.; Roditchev, D.; Stéphant, N.; Troadec, D.; Rozenberg, M. Electric Field Induced Avalanche Breakdown and Non-Volatile Resistive Switching in the Mott Insulators AM₄Q₈. *Eur. Phys. J. Spec. Top.* 2013, 222 (5), 1046–1056. DOI: 10.1140/epjst/e2013-01905-1.
- (19) Stoliar, P.; Rozenberg, M.; Janod, E.; Corraze, B.; Tranchant, J.; Cario, L. Nonthermal and Purely Electronic Resistive Switching in a Mott Memory. *Phys. Rev. B - Condens. Matter Mater. Phys.* 2014, 90 (4), 1–6. DOI: 10.1103/PhysRevB.90.045146.

- (20) Babich, D.; Corraze, B.; Lorenc, M.; Bertoni, R.; Cammarata, M.; Mariette, C.; Servol, M.; Cailleau, H.; Janod, E.; Cario, L.; others. Hot Carriers Generation and Resistive Switching Induced by Electric and Light Pulses in the Mott Insulator GaTa₄Se₈ (Conference Presentation). In *Physics and Simulation of Optoelectronic Devices XXVIII 2020*, 11274, 112740B. DOI: 10.1117/12.2556843.
- (21) Dubost, V.; Cren, T.; Vaju, C.; Cario, L.; Corraze, B.; Janod, E.; Debontridder, F.; Roditchev, D. Resistive Switching at the Nanoscale in the Mott Insulator Compound GaTa₄Se₈. *Nano Lett.* 2013, 13 (8), 3648–3653. DOI: 10.1021/nl401510p.
- (22) Goldstein, J. I.; Newbury, D. E.; Michael, J. R.; Ritchie, N. W. M.; Scott, J. H. J.; Joy, D. C. *Scanning Electron Microscopy and X-Ray Microanalysis*; Springer, 2017. DOI: 10.1007/978-1-4939-6676-9.
- (23) Klapetek, P. *Quantitative Data Processing in Scanning Probe Microscopy: SPM Applications for Nanometrology*; Elsevier, 2018. ISBN: 9780128133477
- (24) Hodoroaba, V.-D. Energy-Dispersive X-Ray Spectroscopy (EDS). In *Characterization of Nanoparticles*; Elsevier, 2020; pp 397–417. DOI: 10.1016/B978-0-12-814182-3.00021-3
- (25) Smith, E.; Dent, G. *Modern Raman Spectroscopy: A Practical Approach*; 2019; Vol. 5. DOI: 10.1002/0470011831.
- (26) Vaju, C.; Cario, L.; Corraze, B.; Janod, E.; Dubost, V.; Cren, T.; Roditchev, D.; Braithwaite, D.; Chauvet, O. Electric-Pulse-Driven Electronic Phase Separation, Insulator-Metal Transition, and Possible Superconductivity in a Mott Insulator. *Adv. Mater.* 2008, 20 (14), 2760–2765. DOI: 10.1002/adma.200702967.
- (27) Rocco, R.; Del Valle, J.; Navarro, H.; Salev, P.; Schuller, I. K.; Rozenberg, M. Exponential Escape Rate of Filamentary Incubation in Mott Spiking Neurons. *Phys. Rev. Appl.* 2022, 17 (2), 024028. DOI: 10.1103/PhysRevApplied.17.024028.
- (28) Tranchant, J.; Querre, M.; Janod, E.; Besland, M. P.; Corraze, B.; Cario, L. Mott Memory Devices Based on the Mott Insulator (V₁-xCrx)₂O₃. 2018 IEEE 10th Int. Mem. Work. IMW 2018 2018, 1, 1–4. DOI: 10.1109/IMW.2018.8388841.
- (29) Dutta, S.; Kumar, V.; Shukla, A.; Mohapatra, N. R.; Ganguly, U. Leaky Integrate and Fire Neuron by Charge-Discharge Dynamics in Floating-Body MOSFET. *Sci. Rep.* 2017, 7 (1), 1–7. DOI: 10.1038/s41598-017-07418-y.
- (30) Claramunt, S.; Wu, Q.; Maestro, M.; Porti, M.; Gonzalez, M. B.; Martin-Martinez, J.; Campabadal, F.; Nafría, M. Non-Homogeneous Conduction of Conductive Filaments in Ni/HfO₂/Si Resistive Switching Structures Observed with CAFM. *Microelectron. Eng.* 2015, 147 (November), 335–338. DOI: 10.1016/j.mee.2015.04.112.

- (31) Zhao, X.; Liu, S.; Niu, J.; Liao, L.; Liu, Q.; Xiao, X.; Lv, H.; Long, S.; Banerjee, W.; Li, W.; Si, S.; Liu, M. Confining Cation Injection to Enhance CBRAM Performance by Nanopore Graphene Layer. *Small* 2017, 13 (35), 1–9. DOI: 10.1002/smll.201603948.
- (32) Babich, D.; Tranchant, J.; Adda, C.; Corraze, B.; Besland, M.-P.; Warnike, P.; Bedau, D.; Bertoncini, P.; Mevellec, J.-Y.; Humbert, B.; Rupp, J.; Hennen, T.; Wouters, D.; Llopis, R.; Cario, L.; Janod, E. Microscopic Identification of the Electric-Field-Driven Insulator to Metal Transition in a Mott Insulator. *arXiv* 2021.
- (33) Li, H.; Zhang, Q.; Chong, C.; Yap, R.; Tay, K.; Hang, T.; Edwin, T.; Olivier, A.; Baillargeat, D. From Bulk to Monolayer MoS₂: Evolution of Raman Scattering. *2012*, No. 1 L, 1385–1390. DOI: 10.1002/adfm.201102111.
- (34) Cortijo-Campos, S.; Kung, P.; Prieto, C.; de Andrés, A. Forbidden and Second-Order Phonons in Raman Spectra of Single and Few-Layer MoS₂ Close to C Exciton Resonance. *J. Phys. Chem. C* 2021, 125 (43), 23904–23910. DOI: 10.1021/acs.jpcc.1c06632.

Statement of non-plagiarism

I hereby declare that all information in this report has been obtained and presented in accordance with academic rules and ethical conduct and the work I am submitting in this report, except where I have indicated, is my own work.

Signature of the student

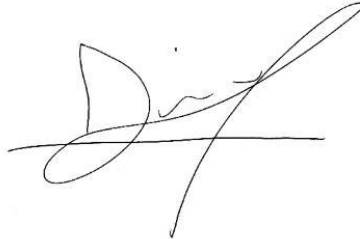
A handwritten signature in black ink, appearing to be 'S. H. H.' with a long horizontal stroke extending to the right.

Supervisor approval

I, the undersigned, Pascale Diener, supervisor of Tushar Chakrabarty, student of the PSRS EMJMD, during his master thesis at Institut d'électronique de microélectronique et de nanotechnologie (IEMN) certify that I approve the content of this master thesis report entitled "Resistive switching in Mott materials".

Date and signature of the supervisor

21-08-2023

A handwritten signature in black ink, appearing to read 'Diener', written over a horizontal line.

Copyright of Figures

In this report, total three figures were taken from other sources. The permission to use these figures on the thesis have been taken from the corresponding publisher. The licences have been uploaded to the drives and it can be accessed by following links:

Permission for Fig. 1.5 :

https://drive.google.com/file/d/1_3TPtr4e2DWFkVycdL9HFstJ_8326ZtM/view?usp=sharing

Permission for Fig. 1.7 :

<https://drive.google.com/file/d/1NYUY1zEvcoZeoFkkF65ewrX59XuLEDxr/view?usp=sharing>

Permission for Fig. 2.16 :

https://drive.google.com/file/d/17pUzfPQMibcRAbN3JSkSRDu_Zlusyhmt/view?usp=sharing